Modeling a Shape Memory Alloy Based Actuator for Aerodynamic Load Control on Aircraft Wings

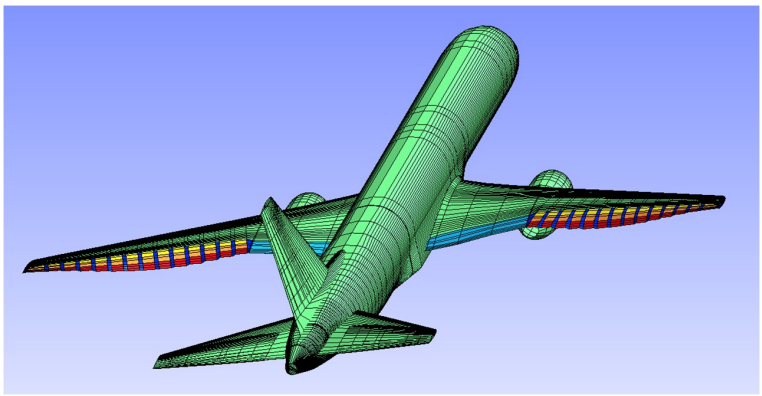

Master Thesis

David Donado Cortés

Supervisors:

Adrián Lara Quintanilla
José Manuel Torralba Castelló

Madrid, February 2015

Title: Modeling a SMA Based Actuator for Aerodynamic Load Control on Aircraft Wings.
Author: David Donado Cortés.
Supervisors: Adrián Lara Quintanilla (TUDelft) / José Manuel Torralba Castelló (UC3M).

COMMITTEE

Chairman: Elena Bernardo Quejido.
Secretary: Paula Álvarez Olmos.
Chair: José Luis Pérez Castellanos.

Master Thesis defended on Wednesday February 18^{th}, 2015. In Leganés, Carlos III University of Madrid, which MARK is

Chaiman

Secretary **Chair**

Resumen

Este Proyecto Fin de Carrera está basado en la investigación de un futuro tipo de alas de avión que son capaces de adaptarse a diferentes condiciones de vuelo: condiciones medioambientales y condiciones de maniobra. En concreto, las alas adaptativas mostradas en este Proyecto se centran en el estudio en el borde de salida del ala. Con ello se pretende modificar su geometría y, por consiguiente, su aerodinámica. Para modificar la geometría del ala, se introducen los materiales inteligentes denominados Aleaciones con Memoria de Forma (Shape Memory Alloys o SMA) en modo de hilos en actuadores poliméricos, que durante su uso inducen la deflexión en el actuador. El objetivo de este Proyecto es describir el comportamiento de estas aleaciones y desarrollar un modelo de simulación que represente su comportamiento. Además se estudia el rendimiento de este material y se compara con los resultados del modelo implementado. Todos estos ensayos confirman que el proceso de enfriamiento del material es el factor meterminante en el proceso.

El primer punto de este Proyecto ha sido desarrollar un modelo de simulación de SMA (single model). Este modelo ha sido implementado en COMSOL siguiendo el modelo desarrollado por Müller Achenbach Seelecke. Este modelo requiere algunos parámetros iniciales referentes al material para su solución, que se obtienen mediante dos ensayos isotermos a diferentes temperaturas y un ensayo isobárico. Los ensayos isotermos proporcionan algunos parámetros geométricos referentes a su comportamiento, mientras que el isobárico hace referencia al coeficiente de transferencia de calor. Con todos estos parámetros, se consiguió que el modelo convergiera correctamente con soluciones satisfactorias y comparables con los ensayos de laboratorio. Así, se aprobó la validación del modelo, empleándolo para analizar el comportamiento en diferentes simulaciones y usarlo como base para el modelo antagonista (antagonistic model). Validado el modelo para un único hilo SMA, se realizaron y compararon diferentes ensayos isobáricos con los resultados obtenidos del modelo. Se analizó así la respuesta del hilo frente a los procesos de calentamiento y enfriamiento para diferentes masas y caudales de aire. Con estos ensayos, se obtuvieron los tiempos de respuesta del hilo SMA (calentamiento y enfriamiento) y, con su combinación, los tiempos de proceso en diferentes situaciones. El máximo ratio de trabajo está limitado por la potencia eléctrica de entrada y el flujo de aire, como se ha observado en los ensayos de laboratorio y de simulación. Comparando ambos resultados, se observaron algunas diferencias. Éstas son debidas principalmente al modelo de simulación implementado, ya que éste es un modelo monocristalino mientras que el hilo real es policristalino. Por ello, el modelo implementado tiene respuestas más rápidas y deformaciones más grandes.

Como se ha comentado anteriormente, el modelo para un único hilo SMA se siguió desarrollando hasta implementar el modelo antagonista (actuador con hilos SMA en su interior desplazados de la fibra neutra con el objetivo de conseguir una deflexión bidireccional). Como en el primer modelo, algunos parámetros fueron necesarios para su simulación. Alguno de éstos fueron importados del primero modelo, mientras que otros fuera calculados, como por ejemplo la influencia del actuador. Además, para que el modelo convergiera, fue necesario un parámetro extra de ajuste, que disminuyera la influencia del actuador. Siendo este parámetro una de las futuras vías de investigación del modelo.

Es importante destacar la importancia del enfriamiento forzado mediante caudal de aire en el comportamiento del SMA en ambos modelos. Ya que la influencia del flujo convectivo en el sistema es hasta 8,5 veces mayor que la convección natural, lo que hace que se consigan impor-

tantes ratios de trabajo de hasta 0,12 Hz en ensayos experimentales o 0,45 Hz en simulación. La diferencia en los resultados se debe principalmente al modelo de simulación implementado, como se ha comentado anteriormente. Por último, el modelo antagonista también muestra resultados satisfactorios comparando los resultados experimentales y de simulación. Este modelo es una futura vía de investigación con el objetivo de entender mejor la influencia del actuador en el sistema, así como su interacción con el resto de parámetros.

Abstract

This Thesis studies a kind of wings that are able to adapt them to different flight conditions: aircraft manoeuvre and environment conditions. The adaptive wings shown here are focused on the trailing edge of the wing. Thus, the aerodynamics of the wing and its surface can be changed. In order to modify its geometry, Shape Memory Alloys are embedded in an actuator, so that a deflection of the actuator can be induced. The goal of this Thesis was to describe the Shape Memory Alloy behaviour and develop a model that was able to provide its behaviour. In addition, the performance of the material was studied and compared with the model results. Those tests confirm that the active cooling is the main actuation factor.

The first point of this Thesis has been the development of a model for a SMA. This model has been implemented in COMSOL, following the the Müller - Achenbach - Seelecke SMA model. In order to run the model, some parameters were required in a SMA wire. Those parameters were obtained by two isothermal tests at different temperatures and isobaric tests. The isothermal tests provided some geometrical parameters about its behaviour, whereas the isobaric tests yielded the heat transfer coefficient. Therefore, the model was run successfully and validated, because the model shows a good agreement with the results obtained by experiments. This model was used to analyse the SMA behaviour at different simulations and implement the antagonistic model.

Once the single model was validated, different isobaric tests were done and compared with the model results. For weights from 1kg to 6kg, the wire was tested analysing the heating and cooling responses. The time that takes for the wire to be contracted and elongated is calculated. Combining them, the maximum working rate was obtained. This rate is limited by the power and airflow, as has been shown in the experimental and simulation results. Some inaccuracies could be appreciated in both results, due to the model implemented. This model is monocrystalline, whereas the real wire is polycrystalline. Therefore, the model has faster responses and higher strains. Moreover, the best strain-area was determined around the midpoint of the strain, where the highest responses were obtained.

Following to the single model, the antagonistic model has been implemented and validated. Some parameters were required to run the model properly. Some of them were imported from the single wire model, and other were calculated, as such the beam influence. In order to get comparable results, a tuning parameter was necessary. This parameter affects to the actuator influence, reducing its influence. This parameter is one of the future work in order to improve the model.

Acknowledgement

First I would like to thank the three people who have made this great experience possible. José Manuel for his help, support and supervision from Madrid, as well as for encouraging and making me see everything that this opportunity could offer me. Irene for introducing me the Delft University of Technology three years ago, and her support and dedication from the beginning. And finally to my supervisor in Delft and friend Adrian, with whom I have struggled every day to get the project done. His advice and dedication have helped me to improve my skills and develop my career.

I would like to thank professor Rinze Benedictus for the opportunity to work in his group. I would also like to acknowledge Gemma and Lissete for their work and dedication, even when my stay in Delft was hanging by a thread.

On a more personal notes, me gustaría darles las gracias a mis padres y hermanos que me han apoyado y aguantado en los momentos difíciles, de más tensión y emoción. Con ellos he sufrido lo que no está escrito. Y por supuesto al resto de mi familia, abuelos y primos.

A todos mis amigos, porque sin todos vosotros, vuestros apuntes y vuestro apoyo, así como los buenos momentos que hemos pasado, no estaría donde estoy. Gracias por todo el apoyo recibido desde España, que han hecho que me sintiera siempre cerca de vosotros. Y a toda la gente que he conocido en Delft, encantadora y que han hecho mi estancia muy especial. En concreto a mis amigos del "fishtank", personas que siempre estarán conmigo.

Y a Pilar, porque tu apoyo ha sido muy importante para mí. Sin ti esta experiencia no hubiera sido lo mismo, lo que he disfrutado y sufrido a tu lado. Después de tanto tiempo esperando ha sido posible realizar nuestro sueño juntos. Y por su puesto a su familia.

Dank u wel. Thank you. Gracias.

Contents

Contents vi

List of Figures viii

List of Tables x

1 Introduction 1
- 1.1 From dreams to reality . . . 1
- 1.2 Nowadays . . . 2
- 1.3 Next step: Smart fixed-wing Aircraft . . . 3

2 Shape Memory Alloys 5
- 2.1 Introduction . . . 5
- 2.2 Material characteristics . . . 6
- 2.3 Cyclical behaviour . . . 9
- 2.4 SMA: How is used and why in a actuator . . . 10

3 Model for a Shape Memory Alloy: implementation in COMSOL and validation 13
- 3.1 Introduction . . . 13
- 3.2 Theory model . . . 14
  - 3.2.1 Implementation in COMSOL . . . 15
- 3.3 Experimental . . . 16
  - 3.3.1 Isothermal tests: Experimental parameters . . . 16
  - 3.3.2 Isobaric tests: Convective heat transfer coefficient . . . 18
  - 3.3.3 Thermal-resistance study: heat losses in the system . . . 22
  - 3.3.4 Equation that governs the heating process . . . 23
- 3.4 Results and discussion . . . 24
  - 3.4.1 Parameters . . . 24
  - 3.4.2 Simulation . . . 26
  - 3.4.3 Validation . . . 26
- 3.5 Conclusions . . . 28

4 Working rate for a SMA: experimental and simulation comparation 29
- 4.1 Introduction . . . 29
- 4.2 Methods and experimental . . . 30
  - 4.2.1 Cooling test . . . 30
  - 4.2.2 Heating test . . . 32
  - 4.2.3 Attainable frequency on a wire . . . 32
- 4.3 Results and discussion . . . 34

4.3.1 Cooling tests . . . 34
4.3.2 Heating tests . . . 35
4.3.3 Working rate . . . 38
4.3.4 Attainable frequency on a wire . . . 38
4.4 Conclusions . . . 40

5 Model validation for antagonistic set up **42**
5.1 Introduction . . . 42
5.2 Theory model . . . 43
5.2.1 Single beam: one-SMA wire and actuator influence . . . 43
5.2.2 Antagonistic beam: two SMA wires and actuator influence . . . 44
5.2.3 Implementation in COMSOL . . . 45
5.3 Experimental . . . 46
5.3.1 Experimental for an antagonistic model: 3 points bending test . . . 46
5.3.2 Comparative tests on an actuator . . . 48
5.4 Results and Discussion . . . 49
5.4.1 Parameters: E_{beam} . . . 49
5.4.2 Actuator influence in an antagonistic setup . . . 50
5.4.3 Validation . . . 51
5.5 Conclusions . . . 53

6 Conclusions **54**

Bibliography **56**

Appendix **58**

A Isothermal Test **58**

B Working rate **61**

List of Figures

1.1 Icarus and Daedalus (1799). Artist: Charles Paul Landon 1
1.2 Comercial Aircraft: AIRBUS A380 2
1.3 Compare the birds wings with the aircraft wings in different flight condition [5] . . 2
1.4 Morphing Wings in the Lockheed Martin Unmanned Air Vehicle (UAV) Concept [19] 3
1.5 Different configuration in the Trailing Edge. Source: Wikimedia Commons 4
1.6 Flaps mechanism: BOEING 787 vs AIRBUS A320. Source:Wikipedia/Author:Julien Scavini 4
1.7 Adaptive wing with servo tab technology [20] 4
1.8 Prototype of compliant structure [21] 4

2.1 Temperature - induced phase transformation of an SMA without mechanical loading [11] 6
2.2 Schematic of the SME. SMA transforming to the detwinned (left), unloading and heating (right), recovering the initial shape [11] 7
2.3 Stress-temperature phase diagram for a SMA [11] 7
2.4 Isobaric and Isothermal test in a SMA to induce the transformation phase [11] . . 8
2.5 Schematic of a stress-strain-temperature curve showing the shape memory effect of NiTi [11] 8
2.6 Pseudoelasctic stress - strain diagram (hysteresis loop) [5] 9
2.7 Training of a SMA wire at a constant temperature [10] 9
2.8 Hysteresis behaviour in a displacement - time graph [10] 10
2.9 Schematics actuator embed SMA wires inside [14] 10
2.10 (a) Antagonistic set up and (b) the actuator [14] 11
2.11 Schematic representation of the actuator deflection [14] 11
2.12 Schematics of the actuator, controller, and inputs and outputs [12] 12
2.13 Response of the actuator at (a) low and (b) high frequency [14] 12
2.14 Relative error observed at different amplitudes and frequencies [14] 12

3.1 Schematics of the isothermal test and its input signal 17
3.2 Experimental isothermal test in order to get the model parameters for T = 363 K 17
3.3 Getting the model parameters from two isothermal tests above T_{A_s} [13] 17
3.4 Schematic of the single wire setup [13] 18
3.5 Dimensions of a module of the actuator 19
3.6 Infrared camera's measuring points. Line 1 and Line 2 measure the wire temperature, and Line 3 checks the beam temperature 19
3.7 Input signals and expected outputs in cooling tests 20
3.8 Fitting curve in Cooling tests 21
3.9 Schema of the heat transfer losses 22

3.10 Configuration of thermal resistances . . . 22
3.11 Example of a fitting curve in a Heating tests . . . 24
3.12 Relationship between the heat transfer coefficient and the airflow . . . 25
3.13 Isothermal test with COMSOL data . . . 27
3.14 Validation of isothermal test, comparing laboratory and COMSOL data . . . 28

4.1 Timing diagram with laboratory data in Cooling tests . . . 30
4.2 Temperature diagram with the maximum decay detected . . . 31
4.3 Strain diagram with the maximum decay detected . . . 31
4.4 Recovery time in temperature diagram . . . 31
4.5 Input signals and expected outputs in heating tests . . . 32
4.6 Timing diagram with laboratory data in Heating tests, including the heating time. 33
4.7 Schema of the attainable frequency study . . . 33
4.8 Timing diagram with COMSOL data (temperature and strain) in Cooling tests . . 34
4.9 Recovery time in strain diagram with COMSOL data . . . 34
4.10 Recovery times for model simulations and experimental tests . . . 35
4.11 Model and experimental results for an isobaric experiment at T = 263K with a mass of 1.25 kg . . . 36
4.12 Timing diagram with COMSOL data in Heating tests . . . 36
4.13 Heating timess for model simulations and experimental data . . . 37
4.14 Model and experimental timing diagram for a isobaric experiment at $T = 263K$ with a mass of $1.25kg$ . . . 37
4.15 Experimental and model attainable working rates (in Hertz) with a load of 1 kg . . 38
4.16 Maximum frequency attrainable for different references . . . 39
4.17 Maximum frequency attrainable for different weights and wires in a midpoint reference. . . . 39
4.18 Thermal influence for working rates with a mass of 1 kg . . . 40

5.1 Model of the wing profile with the actuator on the trailing edge . . . 42
5.2 Schema for a single beam . . . 44
5.3 Schema for anagonistic beam . . . 44
5.4 Schema of the Boundary Condition for antagonistic beam . . . 45
5.5 Actuator tested on a three bending test in the MTS. . . . 47
5.6 Schema of the beam tested on MTS . . . 47
5.7 Schematic of the antagonistic setup . . . 48
5.8 Actuator deflection under a load applied [8] . . . 49
5.9 Fitting of the mass - strain relationship [8] . . . 50
5.10 Schema of a actuator tested in the beam influence study . . . 51
5.11 Antagonistic behaviour: real deflection on the beam . . . 52

A.1 Isothermal test with laboratory data, every temperatures . . . 58
A.2 Isothermal test with COMSOL data, every temperatures . . . 59
A.3 Validation of isothermal test (laboratory and COMSOL), every temperatures . . . 60

B.1 Attainable actuator working rates (Hz) in experimental data . . . 61
B.2 Attainable actuator working rates (Hz) in model data . . . 62

List of Tables

3.1 Equipment used on isobaric tests 20
3.2 Initial data in thermal resistance study 23
3.3 List of model parameters from isothermal test at $T_L = 363K$ and $T_H = 383K$ . . 24
3.4 Measured airflow and fitting results 25
3.5 Results of the total thermal resistance and its influence for each losses way 26

5.1 Actuator deflection for different weights [8] 50
5.2 Simulation results for antagonistic setup 52
5.3 Experimental results for antagonistic setup 52

Chapter 1

Introduction

1.1 From dreams to reality

From the beginning of time, the humans have been obsessed with crossing the skies and searched for many different ways to get it with a single goal: FLY. There are many myths and legends which tell us how the Anticients eluded several situations. One of the most important and famous myths is Icarus and Daedalus, father and son who escaped with wax wings from the Minos Island where they were a prisoners, shown an artistic represention in Figure 1.1.

Figure 1.1: Icarus and Daedalus (1799). Artist: Charles Paul Landon

Turning away from myths and legends, there also are a lot of manuscripts where the first "flights" are told , such as Abbas Ibn Firnas who jumped from a tower in Cordoba (Spain) with a wing-like cloak in 852 AD (one of the first parachutes), or the Montgolfier's brothers who showed their hot air balloon in France in 1782.

The Wright's brothers got the next step when they introduced important concepts: yaw, warp, and sway. Thus, they were able to fly in their first aircraft in December of 1903. From the Wright's brothers, many different changes and technologies have been developed and introduced in the aircrafts. But the most important developments came during the Second War World, where the engineers improved their aircrafts constantly, getting more elevation, longer-haul, increasing the storage and carried capacity, and improving the fighter in a few years, among other improvements.

After the war, the commercial aircrafts came into our life (Figure 1.2). All that time, there were very important changes in the aircrafts to become more efficient and effective: more resistant and lighter materials, fuel optimization, communications, etc. The new reactor and aerodynamic shape were introduced to transport passengers more comfortably and faster as we know it today.

Figure 1.2: Comercial Aircraft: AIRBUS A380

1.2 Nowadays

Until a few years ago, all the companies looked for the most safety, the fastest, and the longest-lasting aircraft. But not only this last technology is used to do the most efficient aircraft nowadays, it is focusing on developing a safety and a environmentally friendly sector, being aware that the Earth's resources are limited and the pollution is causing several damages in our planet.

Many of the improvements are focused on mitigate the climate change, so there are many researches who are developing new techniques and concepts of aircrafts. One of them is the study on the birds flight (which Leonardo da Vinci observed and wrote a book about their flight), because the birds are the most effective flight machines, adapting their wings to the variant flight conditions. Thus the *Morphing Wing* try to become developed in the aircrafts, as in Figure 1.3 .

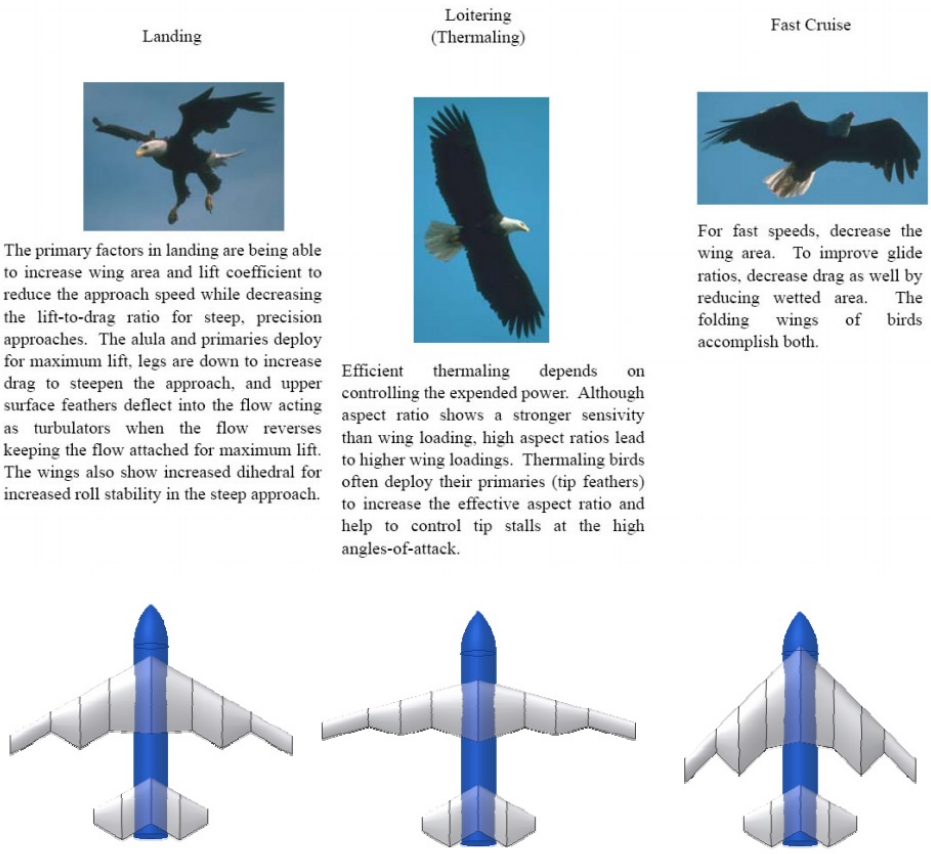

Figure 1.3: Compare the birds wings with the aircraft wings in different flight condition [5]

This idea tries to adapt the wings depending on the flight conditions to increase the lift during take-off and landing, extending them for optimum cruising, or fold them for efficient descent. It is really difficult without increasing the weight with heavy mechanism and materials, as well as the cost involved. This technology has already been developed and mounted a in the Lockheed Martin Unmanned Air Vehicle Concept, as in Figure 1.4. This particular design is inspired from a sea gull as it allows wing folding out of the span plane, putting a part of it inside the fuselage. The problem now is the air flow control, how Wayne Smith explains in [19].

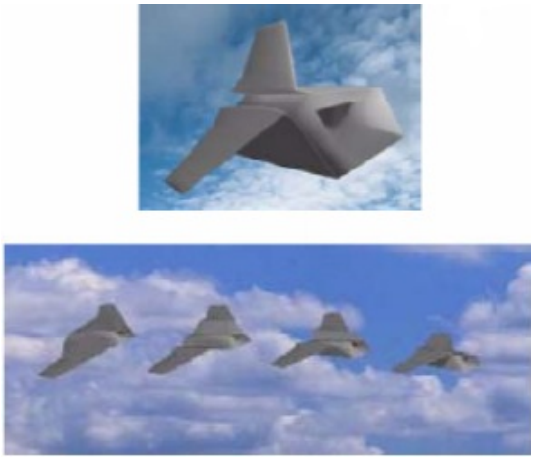

Figure 1.4: Morphing Wings in the Lockheed Martin Unmanned Air Vehicle (UAV) Concept [19]

Nowadays, this kind of aircraft is very difficult to be built due to all the technological and economic difficulties. Therefore a promising solution is the application of deformable and controllable surfaces, which can change the aerodynamics of the wings, resulting in drag reduction and lift increase.

There are a lot of researchers studying Morphings Wings and developing many projects to find the most efficient wing's configuration. This Thesis is focused on the trailing edge of the flap. It explaines how the trailing edge works and the advantages of using continuous wings (without mobile parts). Moreover, which are the possibilities on the trailing edge, how the smart materials can be used to control its shape. The origin of this project is inside a research headed by the tutor of my Thesis, Adrián Lara Quintanilla, PhD researcher at Delft University of Technology.

1.3 Next step: Smart fixed-wing Aircraft

There are many ways where the new technology can be applied to develop controllable wings. A lot of researchers are looking for an efficient configuration and many studies are focused on the leading and the trailing edge. In this thesis a morphing trailing edge is considered.

Several configurations are possible to adapt the trailing edge to the flight conditions. In the actual aircrafts, the flaps and other mobile parts reduce the flight speed while increasing the lift force to land and vice versa for cruising speed, as shown in Figure 1.5 .

Different companies have different flag configurations gaining benefits (Figure 1.6). These kind of wings are not smart fixed-wings, adaptative wings and make use of heavy hydraulic mechanisms.

That discontinuity produces a turbulent flow along the wings which may damage them [2, 1] (fatigue, vibrations...). In order to reduce and control these factors, it is desirable to create continuous wings to achieve a laminar flow. An adaptive wing would be able to reduce it and improve its control. The most important ways Smart Material, Servo Tab and Compliant Mechanisms. Smart Materials are the way developed in this Thesis and its behaviour is explained in Chapter 2. Servo Tab has some advantages and disadvantages: it shows a good adaptively to the flight conditions and laminar flow, but complex and heavy hydraulic mechanisms [20]. Figure 1.7 shows

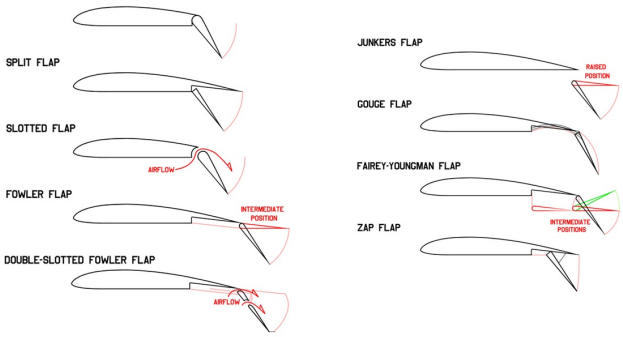

Figure 1.5: Different configuration in the Trailing Edge. Source: Wikimedia Commons

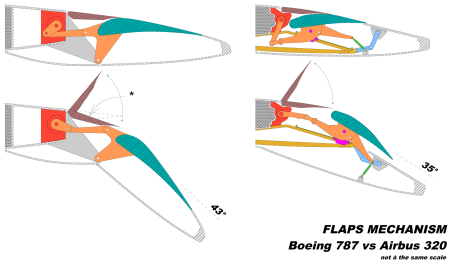

Figure 1.6: Flaps mechanism: BOEING 787 vs AIRBUS A320. Source:Wikipedia/Author:Julien Scavini

this kind of adaptive wings. The Compliant Mechanisms are a kind of mechanism that transmits the motion and force from the elastic deformation of its elements. These mechanisms are a single structure. Therefore, it shows better benefits: simplex, more fatigue resistance,and easier manufacture [20, 21]. One of this prototype monolithic structure is illustrated in Figure 1.8.

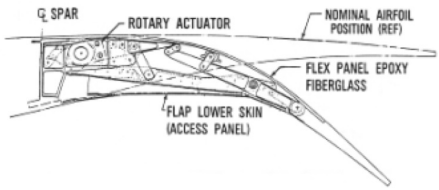

Figure 1.7: Adaptive wing with servo tab technology [20]

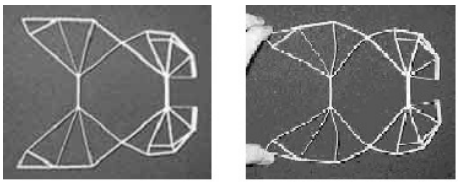

Figure 1.8: Prototype of compliant structure [21]

This Thesis is focused on the adaptive wings in aircrafts. The smart fixed-wings are a reality and there are different ways in order to achieve them. As it has been described, the smart materials are one of these ways, where one of them is embedded in the trailing edges of the flap. The goal of this Thesis is to describe the smart material used (Shape Memory Alloy) on the trailing edge of the flap. Moreover, its behaviour is studied and a model developed, which is implemented and validated in a Finite Element Analysis Software. In addition, the performance of the material is analysed and compared with the model results. In order to improve its performance, different tests have been done, where the active cooling is the main actuation factor. The characterization of the material, model implemented and tests done in this Thesis are explained in next chapters.

Chapter 2

Shape Memory Alloys

2.1 Introduction

Smart materials are used to modify one or more of their properties with an external stimuli such as stress, temperature, electric, magnetic fields,etc. Some of them are common, such as: Shape Memory Alloy (SMA) (in which large deformations can be induced and recovered through temperature changes), Piezoelectric (materials that produce a voltage when stress is applied), and Magnetostrictive (exhibit change in shape under the influence of magnetic field). Most used Smart Materials and different applications are explained by J.L. Pons in [17]. One of these applications is in the aerospace field. The Smart Material can be utilized in different ways in aircrafts, such as SMA in adaptive wings.

Using Shape Memory Alloys in the trailing edges of the flaps, aircrafts have continuous flaps which are able to change their shape to adapt it to the flight conditions. There are many studies about this material because it is light, has a good corrosion properties, and easy and low maintenance, as well as no incompatibly with other material (composites, aluminium, titanium...) or other devices [1]. SMAs have also a fast heating responses with a not too high power consumption, being the slow cooling responses one of the main problem of this Smart Material. The heating and cooling rate are explained in Chapter 4.

Also this kind of wings have a lot of benefits doing it more interesting for our society [1, 2, 5]:

- Estimate fuel savings around 3.5%, in standard flight operations, or up to 5 - 12% on long range operations. Reduction in CO2 and NOx emissions.
- Weight savings, no heavy hydraulic systems. Increase of the aerodynamic efficiency, Drag reduction (around 10% in the aircraft and around 25% in the wing), and Lift increasing.
- Avoid of the extreme loads, according to flight conditions.
- Less fatigue due to less vibrations, reduction around 21%.
- High reliability, with no complex mechanics.
- The maintenance of the mechanisms should be replacing the SMA wires.
- Reduction of aircraft noise by up to 10 dB through engine noise shielding configurations, in particular for business jets.
- High control in aeronautical services, being able to be adapted to different flight conditions.

There are a lot of studies to find the best way to control it, as J.L. Pons explaines in [17]. In this thesis, an actuator will be used to develop a morphing trailing edge. This thesis is focused on understanding the SMA's and actuator's behaviour. For that, it is necessary to do studies of

the Smart Material and develop a good model. In the next sections, why and how the actuator is used and controlled will be explained, as well as the behaviour of the SMA wires in which a large deformation can be induced and recovered through temperature.

2.2 Material characteristics

Shape Memory Alloys (SMA) derive their name from the fact that they are able to memorize a shape. This material was born in 1963 in a study on Ni - Ti alloys, when Beuhler and his co-workers were investigating materials useful for heat shielding. The term Shape Memory Effect (SME) was given to the associated shape recovery behaviour as a material property. There were many studies before with different alloys which showed a shape recovery, but Ni - Ti alloys showed good mechanical properties comparable to other engineering metals with a SME. These materials are used in several fields: aerospace, wind turbine, medical applications, etc. Many of these applications are described in D. Lagoudas's book [11] .

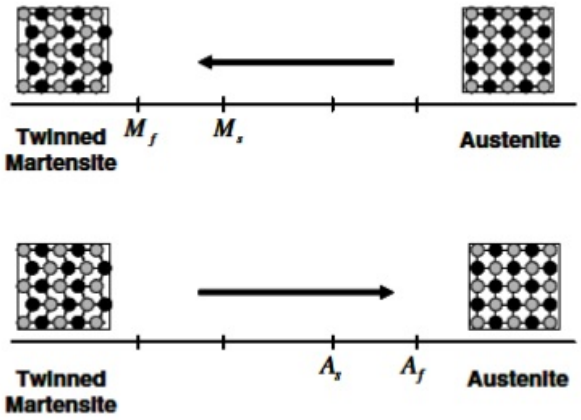

Figure 2.1: Temperature - induced phase transformation of an SMA without mechanical loading [11]

The SMAs have two different phases that depend on the temperature. At low temperatures the material is martensite, having two variants or twins, and at high temperatures it is austenite. The properties of Ni - Ti in its martensite phase and austenite phase are significantly different [11, 17]. When the martensite is heated, it begins to change into austenite, this is called reverse transformation. The temperature at which this transformation starts is called the Austenite Start temperature (A_s). The temperature at which this transformation ends is called the Austenite Finish temperature (A_f). When Ni - Ti in austenite phase is cooled, it begins to transform into martensite. This process is called forward transformation. The temperature at which this transformation starts is called the martensite start temperature (M_s). The temperature at which this transformation finishes is called the martensite finish temperature (M_f). All these process are shown in Figure 2.1 .

A mechanical load in the material can be applied at low temperature (twinned martensite), transforming the crystal structure to detwinned martensite. After releasing the load, the material remains deformed and is able to be heated. Consequently, heating of the material to a temperature above A_f, the reverse phase transformation results (martensite to austenite) and leads to complete the shape recovery, as shown Figure 2.2. In Section 2.4, how the actuator gets this mechanical load will be explained.

Schematic representations of the different phases of the SMA are shown in Figure 2.3, which include the austenitic phase and both the twinned and detwinned martensite, in a stress-temperature diagram showing the transition zones. In order to obtain all of these parameters, two tests can

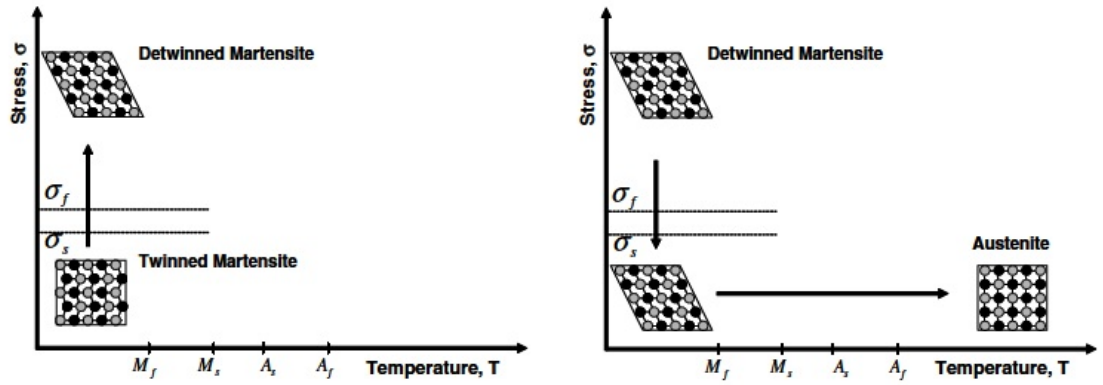

Figure 2.2: Schematic of the SME. SMA transforming to the detwinned (left), unloading and heating (right), recovering the initial shape [11]

be done to find the transition temperatures: isothermal and isobaric tests. In the isobaric test (Figure 2.4a), the transformation phase is induced by temperature when a constant load is applied. And the isothermal test (Figure 2.4b), the pseudoelastic transformation is induced with a constant temperature.

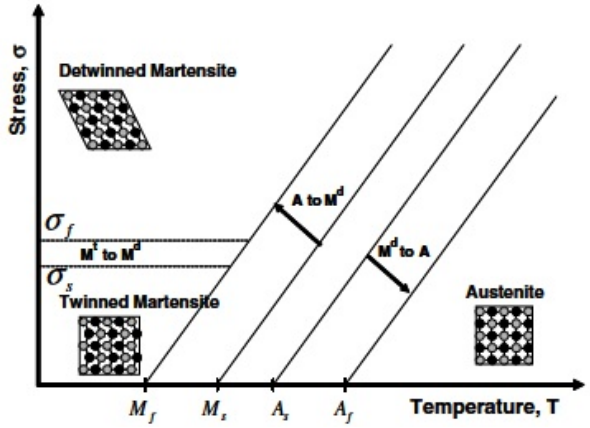

Figure 2.3: Stress-temperature phase diagram for a SMA [11]

Thus, the SMA demonstrates the SME when it is deformed in the martensitic phase and unloaded while the temperature is below M_f. Afterwards the SMA is heated above A_f, recovering its original shape by transforming back into the parent austenitic phase. This transformation can be repeated cycle by cycle. Its behaviour is explained in the Figure 2.5.

The process is explained step by step following the Figure 2.5 [11]:

- Starting from the point A, the SMA is at zero stress. Cooling it below the M_f temperature results in the formation of twinned martensite (point B).
- When the twinned martensite is subjected to a stress that exceeds the start stress level (σ_S), the reorientation process is initiated and the wire increases its length until point C.
- The material is then elastically unloaded from C to D and the detwinned martensitic state is retained.

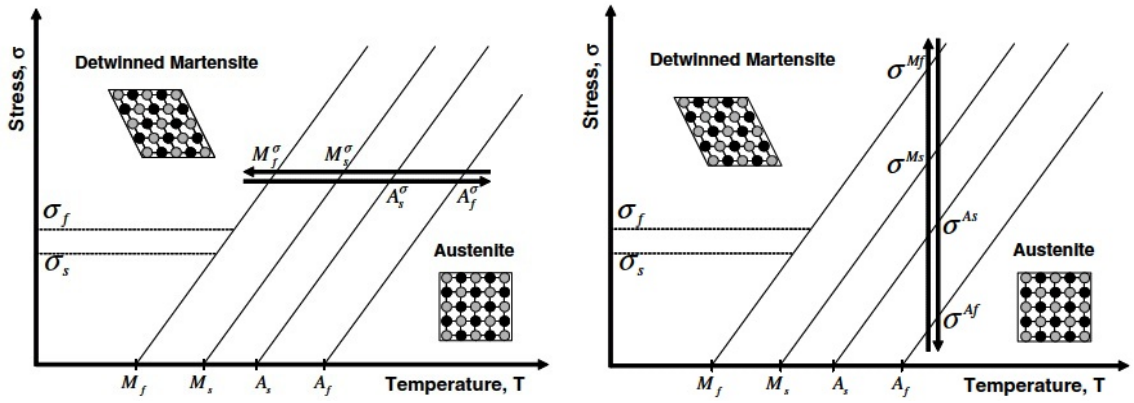

(a) Isobaric test (b) Isothermal test

Figure 2.4: Isobaric and Isothermal test in a SMA to induce the transformation phase [11]

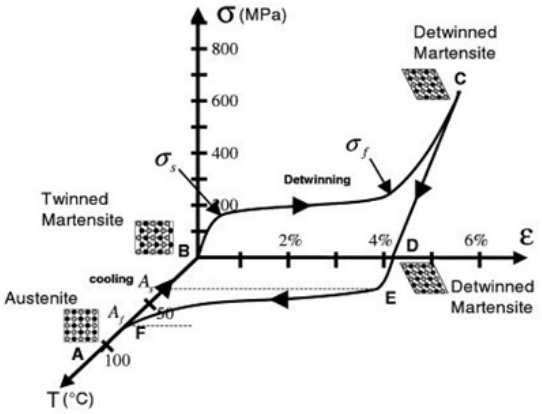

Figure 2.5: Schematic of a stress-strain-temperature curve showing the shape memory effect of NiTi [11]

- Heating the material without any stress, the reverse transformation initiates at A_s temperature (point E), completing it at A_f (point F) where the austenite phase is obtained again. Thus, the wire recover its original memorized length.
- Cooling the material in the absence of stress too, the cycle is closed and the wire is at the initial conditions. A new cycle can be applied.

Thus, a wire in which a previous strain was induced is able to repeat cycles of heating and cooling. In these cycles, a hysteresis loop can be observed (Figure 2.6). This loop appears between two different temperatures, depending on the alloy, what means that the load and unload has different ways, but both finish at the same strain point.

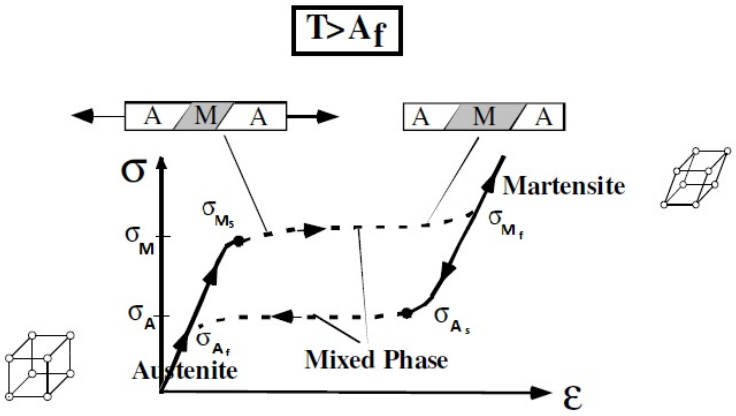

Figure 2.6: Pseudoelasctic stress - strain diagram (hysteresis loop) [5]

2.3 Cyclical behaviour

The pseudoelastic behaviour in the SMAs described previously constitutes an approximation to the real behaviour under applied stress. Actually, only a partial recovery of the strain induced transform by the applied stress is observed. A small outstanding strain remains after each unloading. Thus, the thermo-mechanical cycling of the SMA material results in a training process.

The main result of the training process is the development of Two-Way Shape Memory Effect (TWSME). The TWSME can be observed in SMA when it has undergone repeated thermo-mechanical cycles. After several cycles, the microstructure change and create a macroscopically permanent changes in the material behaviour. In fact, training a SMA corresponds to a process of repeatedly loading the material following a cyclic thermo-mechanical loading path until the hysteric response of the material is stabilized. That is the goal of training the SMA. A huge hysteresis for an actuator is not interesting because the actuator would have an accuracy lost [10].

These permanent defects create a residual internal stress, facilitating the formation of preferred martensitic variants when the SMA is cooled in the absence of external loads. If the internal stress is modified for any reason (aging at high temperature or mechanical overload), the TWSME is perturbed.

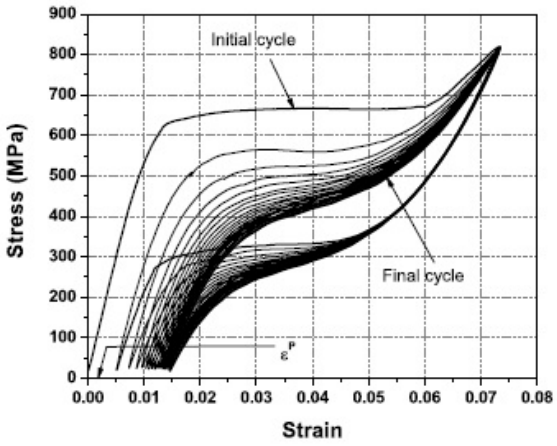

Figure 2.7: Training of a SMA wire at a constant temperature [10]

Isothermal and isobaric tests can be used to train the SMA. In the case of cycling a SMA with a mechanical load under a constant temperature (isothermal test), only a partial recovery

of the strain, generated during unloading, is observed in Figure 2.7. In order to know what is this difference between cycles and when it is stabilized, the time evolution of the displacement is used showing a training wire. The SME loses are observed in the Figure 2.8, where it is stabilized around 5000 cycles after the beginning of the test.

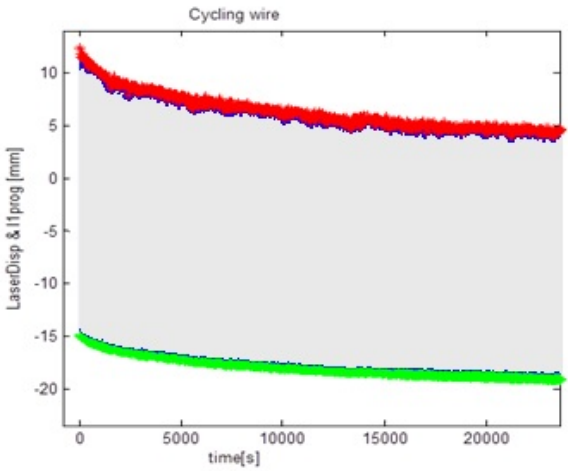

Figure 2.8: Hysteresis behaviour in a displacement - time graph [10]

In conclusion, the results of test demonstrate that the wires lose their SME after the barrier 5000 cycles. After that, it is stabilized and keeps its behaviour. The reduction of SME is 22%. After about 5000 cycles, the wire is ready to be used without any SME reductions [10]. The wire is not able to recover its plastic strain every cycle and is stabilized when the number of cycles increase.

Described the SMA behaviour and its particularities, how the wire is used in a actuator and how it works are explained in next section.

2.4 SMA: How is used and why in a actuator

Before manufacturing the final actuator, a proof - of - concept was carried out to demostrate its feasibility. There have been investigations into the feasibility of the concept, the aerodynamics and control system, as A. Lara-Quintanilla shows in [14]. This thesis is focused on the trailing edge, an actuator in antagonist set up is used (Figure 2.9). This concept is to embed SMA wires in a beam or plate-like structure inside channels. SMA wires were previously prestrained and attached to the beam, recovering their original shape upon heating them.

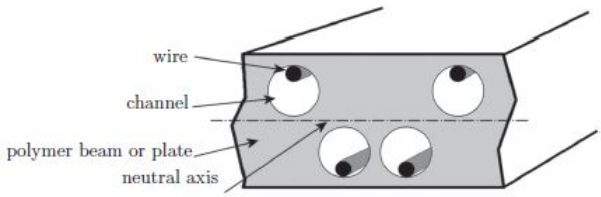

Figure 2.9: Schematics actuator embed SMA wires inside [14]

The channels are off the neutral axis of the actuator, and the wires are placed on the outest part of the channel, as shown in the Figure 2.9. Also, air -or any other fluid - can be forced through the channels. By using this air, higher working rates are expected. The limit bending depends on the beam material which is made out of pure polymer, Anionic Polyamide - 6 (APA - 6). The

most important characteristics are its low Young's modulus and its high level of formability. More characteristics about the material and its manufacturing are described in [14, 3, 22].

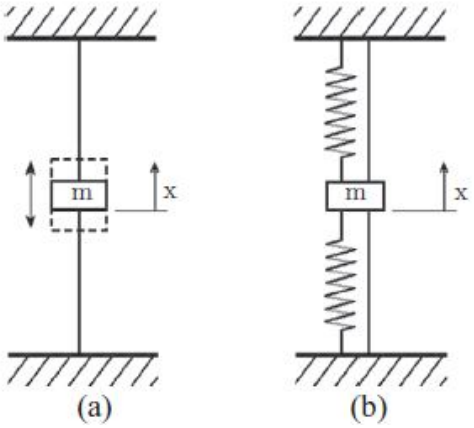

Figure 2.10: (a) Antagonistic set up and (b) the actuator [14]

The antagonist set up is a specific configuration to regain the prestrain of one wire when the opposite one is heated, the actuator can therefore bend in two directions. A schematic representation of this concept can be observed in the Figure 2.10. Following the wire's cycles described in Section 2.1, while one of the wires is heated bending the actuator in this set up, the other one is cooled, regaining the prestrain necessary to be heated and recover its shape afterwards. These deflections are showed schematically in the Figure 2.11.

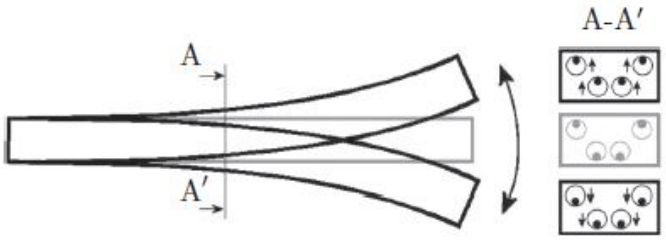

Figure 2.11: Schematic representation of the actuator deflection [14]

With this design, the wires are embedded inside the actuator and bend it. Controllers for the actuator were studied previously [12]. In this actuator, a fuzzy logic controller was implemented. The fuzzy logic controller was motivated by the non-linear characteristics of the system and the complex and multiple outputs needed to control the deflection of the actuator. The actuator's controllers are complex and difficult to explain in a few words and these are not the goal of this thesis. This previous work is explained in [12]. A schematic view of the actuator and its controllers are shown in Figure 2.12 .

In order to investigate the performance of the actuator's controller (antagonistic set up), a new and simple set up was done as shown Figure 2.10 (a). This study was done in a previous work and is explained for different working rates in [14]. The conclusion of this study are: the controller failed in controlling the set-up for high frequencies and amplitudes (Figure 2.13), but the error remained is small for all the frequencies up to 1Hz, as shown Figure 2.14, and the importance of the active cooling. This means that it is interesting to do a study of this kind of actuator, because the actuator is controlled successfully and allowed to work with a good bandwidth.

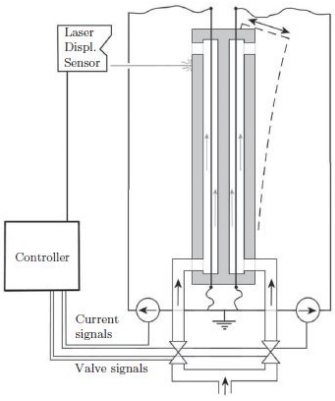

Figure 2.12: Schematics of the actuator, controller, and inputs and outputs [12]

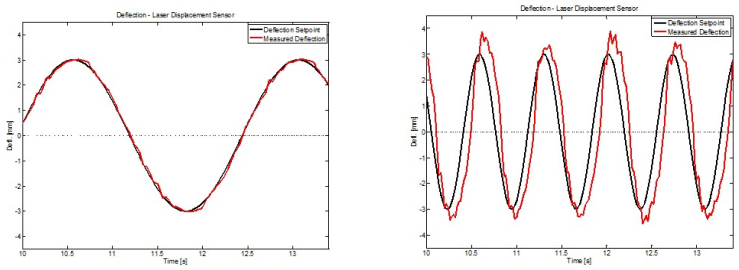

(a) Low frequency (b) High frequency

Figure 2.13: Response of the actuator at (a) low and (b) high frequency [14]

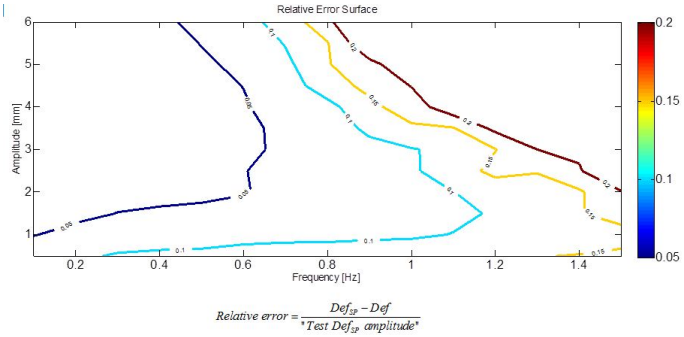

Figure 2.14: Relative error observed at different amplitudes and frequencies [14]

The material (APA-6), actuator and controllers have been described in this chapter. Next chapters show the model that has been implemented and validated, as well as different the cooling and heating tests. Those tests provide the maximum working rate in the actuator. Moreover, the antagonistic setup is developed. All these work validate a model of the actuator and compare the results with its real behaviour, being the goal of this Thesis. The model is implementing in COMSOL Multiphysics®Software and develops in depth in the next chapters (process, parameters, previous studies...).

Chapter 3

Model for a Shape Memory Alloy: implementation in COMSOL and validation

This chapter describes a model for a SMA wire. In order to find a good model, a review of some SMA models is explained, determining the model implemented in this Thesis. Also, the experimental necessary parameters to run the model are obtained. Finally, the validation for the model is done, comparing experimental and simulation tests.

3.1 Introduction

The SMA behaviour explained in Chapter 2 is developed here. The goal of this chapter is to find a good model to describe this alloy due to its good material properties. The SMA has good thermo - mechanical properties. Therefore, the stress, strain and temperature are internally associated, although their relationship is non - linear, as has been described previously.

Moreover, having a good model shows better advantages comparing them with the experimental studies. The model is able to replace those experimental tests with simulations, analysing the SMA in different situations or hypothetic configurations. Other reason to find a good model is the economic issue. The validation for a model is completely necessary nowadays, where the viability of the projects is determined by the investment that has to be done. Therefore, this achievement decreases those investments in a projects that uses SMA wires.

Many different models have been developed during those last years, focused on a one -, two - or three - dimensional models. A historical summary of SMA models and their features is shown in Lagoudas's book [11], with which many researches have developed models in different ways or improved the previous ones.

In this Thesis, an one - dimensional model is implemented. This model was initially proposed by Achenbach [4] and expanded by Seelecke and Müller [18]. This model shows some advantages and captures the SMA behaviour well. One of these advantages is the simplicity to achieve the parameters of the SMA that are necessary for the model. In order to obtain those parameters, only two strain - stress tests at two different temperatures must be done, as explained by Crews et al. in [7]. Moreover, the chosen model shows a favourable computational efficiency [9], not taking long converging times.

For these reasons, the Müller - Achenbach - Seelecke SMA model has been implemented and explained in detail.

3.2 Theory model

The Müller - Achenbach - Seelecke SMA model is implemented and explained in detail. This monocrystal model is based on the phase fraction of martensite (M+ and M-) and austenite (A), representing the proportion of each phase in the SMA. All of the phases can be present at the same time, and therefore the sum of those proportions is the unit.

$$1 = x_A(t) + x_{M+}(t) + x_{M-}(t) \tag{3.1}$$

In Equation 3.1 , x_A is the austenite fraction and x_M is the martensite fraction. The sign is due to tensile or compressive stresses induced respectively. The dynamics of each phase fraction are governed by

$$\dot{x}_{M+}(t) = x_A(t)\, p_{A\to M_+}(T,\sigma) - x_{M+}(t)\, p_{M_+\to A}(T,\sigma) \tag{3.2}$$

$$\dot{x}_{M-}(t) = x_A(t)\, p_{A\to M_-}(T,\sigma) - x_{M-}(t)\, p_{M_-\to A}(T,\sigma) \tag{3.3}$$

where $p_{i\to j}$ $(i,j = A, M_+, M_-)$ are the phase transition rates. These rates are the probability of changing a particle from its current phase (i) to an adjacent one (j), in other words, the probability between A to M_+ or M_- and vice versa. The probabilities are governed for the internal transformations from different phases. The free Gibbs energy and Helmoltz energy control those changes, as shown Jordan E. Massad and Ralph C. Smith in [16].

The overall strain on the wire (ε) depends on the phase structures and their strain (ε_A, ε_{M_+} and ε_{M_-}). Therefore, each phase have their own Young's modulus E_A and E_M. Equation 3.4 shown this strain on the wire.

$$\varepsilon(t) = x_A(t)\,\varepsilon_A + x_{M+}(t)\,\varepsilon_{M+} + x_{M-}(t)\,\varepsilon_{M-} = x_A(t)\,\tfrac{\sigma}{E_A} + x_{M+}(t)\left(\tfrac{\sigma}{E_M} + \varepsilon_T\right) + x_{M-}(t)\left(\tfrac{\sigma}{E_M} - \varepsilon_T\right) \tag{3.4}$$

where ε_T is the maximum recoverable strain. Solving Equation 3.4 for the applied stress σ, the relationship between stress and strain can be deducted:

$$\sigma(t) = \frac{\varepsilon(t) - \varepsilon_T\left(x_{M+}(t) - x_{M-}(t)\right)}{\frac{1-x_{M+}(t)-x_{M-}(t)}{E_A} + \frac{x_{M-}(t)+x_{M+}(t)}{E_M}} \tag{3.5}$$

In this model, regarding the heat, the energy source is Joule heating $j(t)$, and the only heat losses are due to convective transfer h_{conv} and the latent heats $h_{M_\pm}$-h_A. The heat losses are explained in Subsection 3.3.3, and why only the convective heat transfer has been token into account in the model. Those latent heats are due to transformations between the different phases. Further information about the latent heats can be found in [15, 16]. Thus, the temperature evolution on the wire is:

$$\rho_{SMA} c_p \dot{T}(t) = -h_{conv}\left.\frac{A_{SMA}}{v_{SMA}}\right|_{cil}(T(t) - T_\infty) - (h_{M+} - h_A)\,\dot{x}_{M+}(t) - (h_{M-} - h_A)\,\dot{x}_{M-}(t) + j(t) \tag{3.6}$$

where ρ_{SMA} is the density of the SMA wire, c_p is the heat capacity, h_{conv} is the convective heat transfer coefficient, the coefficient $\left.\frac{A_{SMA}}{v_{SMA}}\right|_{cil}$ is the area-to-volume and T_∞ is the room temperature.

Finally, the stress is assumed to be uniform along the wire $\left(\frac{\sigma(x)}{\partial x} = 0\right)$, and it is built the system of the equations that controls the time evolution of the SMA performance:

$$\begin{cases} \dfrac{\sigma(x)}{\partial x} = 0 \\ \dot{x}_{M+}(t) = x_A(t)\, p_{A\to M_+}(T,\sigma) - x_{M+}(t)\, p_{M_+}(T,\sigma) \\ \dot{x}_{M-}(t) = x_A(t)\, p_{A\to M_-}(T,\sigma) - x_{M-}(t)\, p_{M-}(T,\sigma) \\ \rho_{SMA} c_p \dot{T}(t) = -h_{conv} \left.\dfrac{A_{SMA}}{v_{SMA}}\right|_{cil} (T(t) - T_\infty) - (h_{M+} - h_A)\,\dot{x}_{M+}(t) - (h_{M-} - h_A)\,\dot{x}_{M-}(t) + j(t) \end{cases} \tag{3.7}$$

This system of equations together with Equation 3.5 describes the SMA behaviour. Also, the equations allow to calculate the strain, phase fractions and temperature at the same time. Therefore, this model is able to perfom the stress - strain test (isothermal test) and temperature - strain test (isobaric test), comparing its results with experimental tests.

3.2.1 Implementation in COMSOL

The system of ordinary differential equations (ODEs) has been implemented in COMSOL Multiphysics®. This software is a Finite Element Analysis software where simulations with different physics are possible at the same time. Also, mathematical simulations can be done implementing its ODEs. The adaptation of the model equations to the software equations is explained by Crews in [6]. One of the COMSOL possibilities is the partial differential equations (PDE's). Its general form is

$$e_a \cdot \frac{\partial^2 u}{\partial t^2} + d_a \cdot \frac{\partial u}{\partial t} + \nabla\Gamma = f \tag{3.8}$$

The different terms in Equation 3.8, with the real terms into them, are detailed as follows

$$e_a = 0 \tag{3.9}$$

$$u = \begin{bmatrix} u_x \\ x_+ \\ x_- \\ T \end{bmatrix} \tag{3.10}$$

$$d_a = \begin{bmatrix} 0 & 0 & 0 & 0 \\ 0 & 1 & 0 & 0 \\ 0 & 0 & 1 & 0 \\ 0 & h_{M+} - h_A & h_{M-} - h_A & \rho_{SMA} \cdot C_p \end{bmatrix} \tag{3.11}$$

$$\Gamma = \begin{bmatrix} \sigma \\ 0 \\ 0 \\ 0 \end{bmatrix} \tag{3.12}$$

$$f = \begin{bmatrix} 0 \\ x_A(t)\, p_{A\to M_+}(T,\sigma) - x_{M+}(t)\, p_{M_+\to A}(T,\sigma) \\ x_A(t)\, p_{A\to M_-}(T,\sigma) - x_{M-}(t)\, p_{M_-\to A}(T,\sigma) \\ -h_{conv} \left.\frac{A_{SMA}}{v_{SMA}}\right|_{cil} (T(t) - T_\infty) + j(t) \end{bmatrix} \tag{3.13}$$

In order to run the simulation, it is necessary to define the following conditions:

- Adiabatic thermal boundary conditions, namely without heat flux between the wire and the clamps that grip it.

- No boundary conditions in the phase fractions.
- The displacement is gotten at the fix end of the wire, because the first end is built in. Depends on the test, its expression is different. For stress - strain test (isothermal test), the displacement on the free end of the wire is $\Delta L = L_0 \cdot \varepsilon(t) = L_0 \cdot u_x$, where L_0 is the initial length of the wire. For strain - temperature test (isobaric test), a constant stress σ is defined on the free end of the wire.
- The initial conditions for the phase fractions depend on the temperature and stress of the test, as was showed in Figure 2.4 .

As it has been explained, there are many parameters that are necessary to run the model. Some of them are material properties, and others are parameters for the model. Those parameters have been obtained experimentally and are explained in Section 3.3.

3.3 Experimental

This section describes the calculation of the parameters in order to run the model properly and also the experiments that were carried out to get them. Some of them are the material properties, and the other ones the parameters for the model, as it has been shown in the previous section. The material properties which are required are the density and specific heat, which are provided by the manufacturer. Regarding to the parameters for the model, $T_L, E_A, E_M, \sigma_L, \Delta\sigma_L, \sigma_R$, ε_T and h_{conv} were obtained experimentally. All of them were obtained by two isothermal tests on the wire, except the h_{conv}. This h_{conv} was achieved running a isobaric test. Those different test are explained in detail in Subsection 3.3.1 and Subsection 3.3.2 respectively.

Moreover, a thermal study in the system was done. This study is explained in Subsection 3.3.3 and guaranties that the convective heat transfer is the most significant heat loss, ignoring other heat losses. Finally, the equation that governs the heating on the wire is shown. Although this equation is not necessary for any parameters, it gives a better understanding of this process is required. Subsection 3.3.4 explains the parameters of which the temperature depends on the heating process.

3.3.1 Isothermal tests: Experimental parameters

As it has been described, some parameters are required to run the model. Those parameters are $T_L, E_A, E_M, \sigma_L, \Delta\sigma_L, \sigma_R$ and ε_T, and were obtained running two isothermal test, as Crews describes in [7].

This work was done previously and carried out using a Mechanical Testing System (MTS). In order to keep the isothermal conditions on the wire, a Thermotron FR-1-CH-LN2 environmental chamber was used during the experiments. This chamber has two holes through which the gripping system can be introduced into it, holding the wire. Because of this, adiabatic conditions were imposed.

In order to run the test properly, a triangular strain input was applied, analysing its behaviour by strain control. Thus, these tests were run with a positive and negative slopes of strain, getting positive triangles (tensile tests). The maximum of this input is the maximum strain which wants be induced in the wire, whose length was 200mm, and the time per triangle. This experiment and its inputs are shown schematically in Figure 3.1.

This experiment was run for different temperatures above the T_{A_f}. These temperatures were chosen from 363K to 403K, every 5K, with the same input signal, maximum strain induced of 7% on a wire of 200mm length, and 60 seconds per triangle.The result for one of these experiments is shown in Figure 3.2.

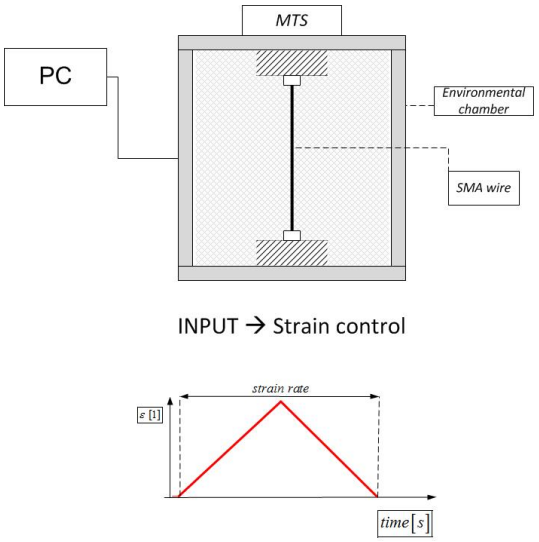

Figure 3.1: Schematics of the isothermal test and its input signal

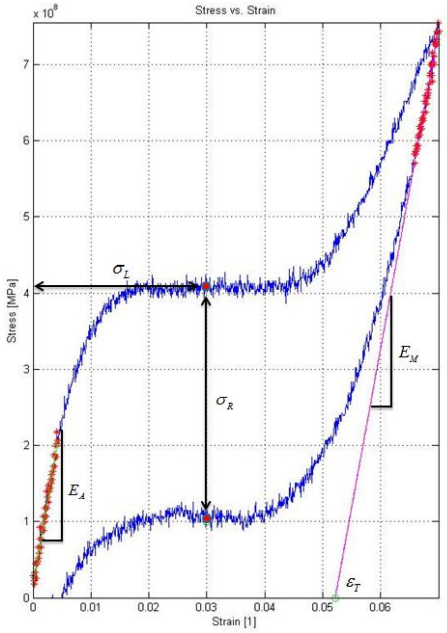

Figure 3.2: Experimental isothermal test in order to get the model parameters for T = 363 K

In Figure 3.2, E_A is calculated as the slope at the beginning of the experiment; E_M is the slope at the beginning of the way back; ε_T is the point in the strain axis from where is calculated E_M being the point of the intersection of the axis; σ_R is the width of the stress hysteresis loop; σ_L is the higher point in this loop; and T_L is the temperature of the experiment at the lower temperature. The last necessary parameter is $\Delta\sigma_T$, which has its own test to get it, following the method proposed by Crews et al. in [7]. Two isothermal experiments are required at different temperatures above T_{A_s}. Those temperatures chosen have been 368K and 383K respectively, as shown Figure 3.3 .

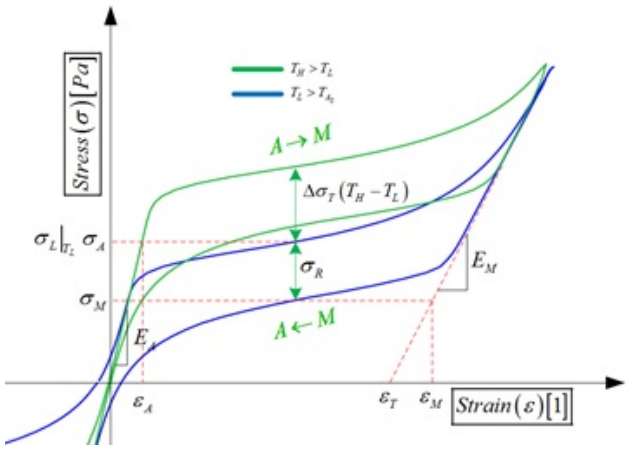

Figure 3.3: Getting the model parameters from two isothermal tests above T_{A_s} [13]

where T_L is the lowest of the two temperatures, T_H the highest one, and $\Delta\sigma_T$ is the maximum stress difference of both of loops. This value is the relation between two tests at different

temperatures, being a constant value.

3.3.2 Isobaric tests: Convective heat transfer coefficient

As it has been described, the convective heat transfer coefficient is calculated with the isobaric setup. Those tests allow to test the wire under a constant load (isobaric test). The variations of the temperature on the wire are possible modifying the power across the wire (Joule effect). Thus, the wire can be heated up, analysing its behaviour when the wire is cooling down it. The active cooling is the crucial key of this actuator. Its influence depends on the convective heat transfer coefficient. Different applied airflows change this coefficient, and also the time that the wire takes to recover its strain. This last point is explained in Chapter 4.

In order to analyse the convective heat transfer coefficient, the SMA wire was embedded inside the channels of the actuator. This setup consists of holding the actuator with clamps in a vertical position. Because of this configuration, the isobaric setup was implemented, hanging different weights on the wire. Those weights were hung where the wire started the way back. Also, a Linear Variable Differential Transformer (LVDT) was used to measure the displacement and, consequently, the strain of the SMA. The electrical connections were done on the top of the actuator, as well as the pneumatic connection. Thus, the forced airflow crossed the actuator from the top to the bottom. Finally, an infrared camera was used to measure the temperature on the wire when the current flows through it, as well as the temperature of the beam. A schema of this configuration is shown in Figure 3.4.

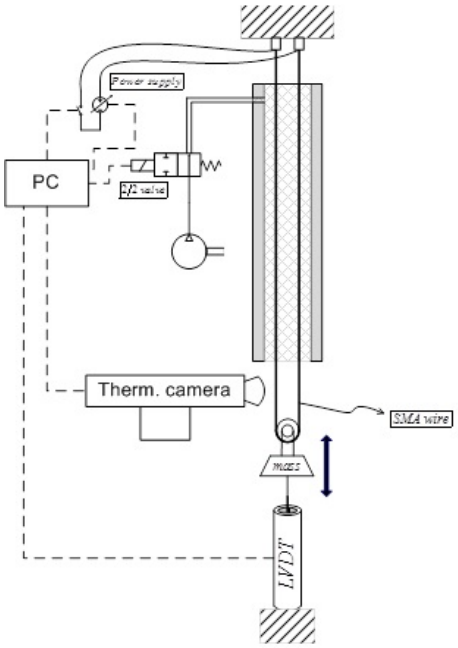

Figure 3.4: Schematic of the single wire setup [13]

Similar thermal conditions than the real ones were wanted during the tests. Therefore, the wire was tested inside the real actuator. The channel has a rectangular section of 10mm width, 0.5mm height and 200mm length. The actuator can be divided in four similar modules with a couple of channels. A schema with the dimensions for a single module is shown in Figure 3.5.

The thermal conditions were important during the test, overall at the beginning of each test and before a new cycle. The starting temperature on the wires and actuator must be the same temperature (room temperature), as well as when a cycle has been finished and is ready to be heated again. Figure 3.6 shows how the temperature was analysed. Three measuring points can

be seen: Line 1 measured the temperature along the wire and is used in the calculus, Line 2 measured the temperature in the way back to be able to compare it visually with the first one, and Line 3 checked the temperature of the beam to begin each experiment at room temperature.

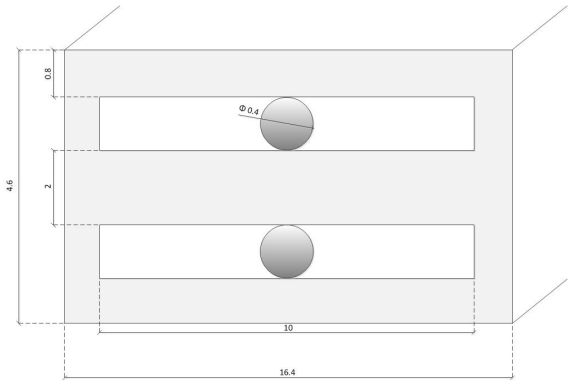

Figure 3.5: Dimensions of a module of the actuator

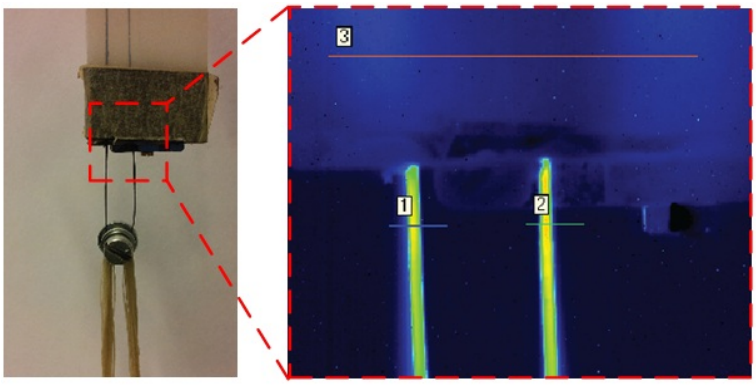

Figure 3.6: Infrared camera's measuring points. Line 1 and Line 2 measure the wire temperature, and Line 3 checks the beam temperature

Moreover, these LVDT data and the infrared camera have been used to calculate the maximum cooling and heating rate in the actuator getting the maximum working rate on the wire. This process is explained in Chapter 4.

The electrical power and the airflow described and the rest of the electronic actuators were controlled by a PC running LabVIEW ®. Those devices are listed on Table 3.1.

Equipment	Model	Manufacturer
DC Power Supply	SM 120-50 DC Power Supply	Delta Elektronika BV
Valve	2/2-way proportional valve Type 2826	Bürket Fluid Control Systems
Infrared camera	FLIR SC7000 Series	FLIR
LVDT	SE 373/50	SE Labs
Flow meter	Molded Flow meter Series MR3000	Key Instruments
Data acquisition	NI 9215 - Analog Input Module	National Instruments
Power supply and valve control	NI 9263 - Analog Output Module	National Instruments

Table 3.1: Equipment used on isobaric tests

As it was described previously, the wire was heated up by keeping a constant power. That heated the wire above T_{Af}. This power was cut off at the same time that the valve was opened, cooling the wire with different flowrates. Those aperture of the valve were from 0V (natural convection) to 5V (forced convection). A timing diagram with inputs (Joule and valve aperture) and expected outputs (temperature and strain) is shown in Figure 3.7.

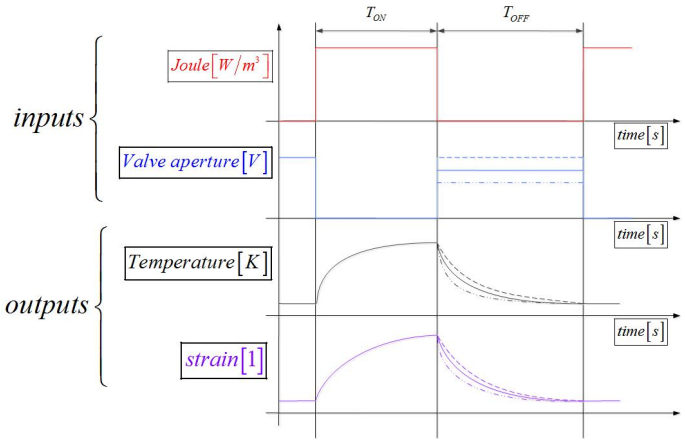

Figure 3.7: Input signals and expected outputs in cooling tests

In order to calculate h_{conv}, the temperature decay had to be analysed. Moreover, a fitting equation that governs the cooling behaviour is found. The heat loss during a convection phenomenon is given by

$$\dot{q} = -h_{conv} \cdot A_{SMA} \cdot (T_{SMA} - T_{\infty}) \tag{3.14}$$

where T_{SMA} is the current temperature of the wire. A uniform temperature on the wire is assumed. Thus, the differential time evolution of the wire's temperature is governed by

$$\frac{dT_{SMA}}{dt} = \frac{\dot{q}}{v_{SMA} \cdot \rho_{SMA} \cdot C_p} \tag{3.15}$$

Equation 3.15 can be solved for T_{SMA}, what gives way the following time evolution of the temperature:

$$T_{SMA}(t) = T_{\infty} + (T_0 - T_{\infty})\, e^{\frac{-h_{conv} A_{SMA}}{v_{SMA} \rho_{SMA} c_p} t} \tag{3.16}$$

where T_{∞} is the room temperature, what is the same that the airflow's temperature, T_0 is the temperature at $t = 0$. Equation 3.16 can be fitted to an exponential equation of the type

$$y = y_0 + ae^{bt} \tag{3.17}$$

All the parameters in Equation 3.16 are known except h_{conv} Therefore, it can be deducted from the coefficient b in Equation 3.17, and the natural and forced convection calculated. The maximum temperature decay detected previously has been used to fit its data to Equation 3.17. The fitting curves show an excellent agreement with the experimental data, as shown in Figure 3.8.

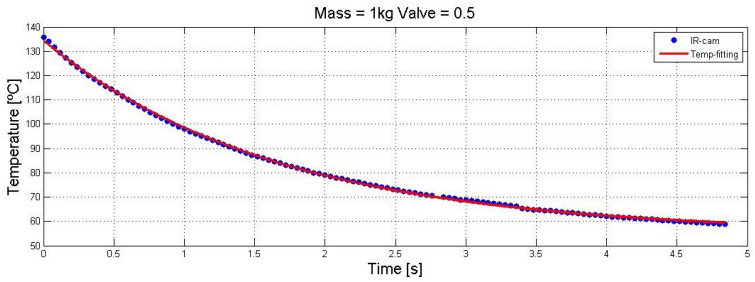

Figure 3.8: Fitting curve in Cooling tests

3.3.3 Thermal-resistance study: heat losses in the system

Initially, conductive and convective losses were taken into account in the actuator. A heat transfer study has been done to determine what was the influence of each one. As it has been explained, the antagonistic setup has different channels above and under the neutral axis (Figure 2.9). While a wire in one side of the neutral axis is heated, the other wire is cooled. Due to this, the heated wire can be considered the origin of the heat and locate it as a heat supply, as Figure 3.9 shown schematically.

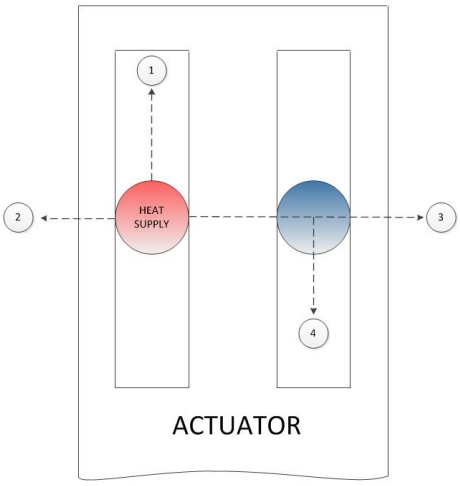

Figure 3.9: Schema of the heat transfer losses

A heat transfer study was done, replacing the conductive and convective states by its thermal resistance. Following the different heat losses ways and taking as reference the room temperature, there were three ways: a convective heat transfer and two conductive heat transfers. The channel was assumed to be at room temperature. This thermal-resistance study is shown in Figure 3.10.

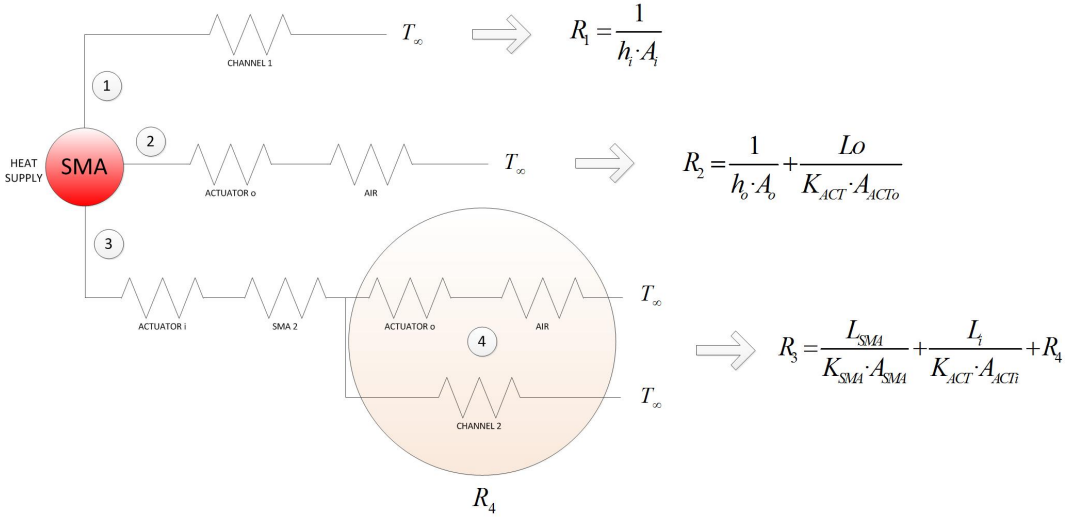

Figure 3.10: Configuration of thermal resistances

In order to calculate the total thermal resistance, the actuator's dimensions were necessary in the equations, as it can be seen in Figure 3.10. A schema of the actuator dimensions is shown in Figure 3.5. Only a module with two channels was used because no heat transfer in transversal

h_e	116	[W/m^2K] Natural convection
K_{ACT}	0.2	[W/mK] Thermal conductivity of the APA-6
K_{SMA}	18	[W/mK] Thermal conductivity of the AUSTENITE
R_{SMA}	0.0002	[m] Radio
L_o	0.0008	[m] Exterior lenght of the actuator
L_i	0.002	[m] Interior length of the actuator
W	0.01	[m] Width of the channel
L	0.26	[m] Length of the wire in mm
α	10%	Percentage of the wire in contact with the actuator
Surfaces		
$A_o = W.L$	0.0026	[m^2] Exterior surface of the actuator
$A_{ACT} = \alpha.2.\pi.R_{SMA}.L$	0.0026	[m^2] Surface in contact with the wire
$A_i = (2.\pi.R_{SMA} - \alpha.2.\pi.R_{SMA}).L$	$3.1.10^{-4}$	[m^2] Surface in contact with the air inside the channels

Table 3.2: Initial data in thermal resistance study

way was assumed. This happens because the thickness is bigger in that way. Also, some extra information was required: actuator properties, surfaces, lengths of the transfers, percentage of the wire's surface that is in contact with the actuator, etc. This information is explained in detail on Table 3.2.

3.3.4 Equation that governs the heating process

Once the tests were done, the equation which governs the heating process was calculated. This equation was not necessary for any parameters in the model, but a better understanding about the heating behaviour was wanted. Thereby, the temperature evolution equation was obtained and also the parameters which depend on the temperature. The heat evolution in a constant power supply is given by Equation 3.18.

$$P = mC\frac{dT}{dt} \tag{3.18}$$

where P is the power, m the mass of the wire, C is the specific heat of the material, and T the temperature. Considering that there are heat losses by convection, a new equation governs the process.

$$P = mC\frac{dT}{dt} + h_{conv}A\left(T - T_{air}\right) \tag{3.19}$$

where h_{conv} is the convective heat coefficient. In this case, the coefficient is the natural convection, due to the forced air is cut off while the power supply is on, as has been described previously. Assuming now that the temperature is uniform along the wire, the differential time evolution of the wire's temperature is governed by Equation 3.20.

$$\frac{dT}{dt} = \frac{P}{mC} - \frac{h_{conv}A}{mC}\left(T - T_{air}\right) \tag{3.20}$$

Thus, Equation 3.20 can be solved for T_{SMA}, what yields the following time evolution of the temperature:

$$T_{SMA} = T_{air} + \frac{P}{h_{conv}A}\left[1 - e^{\left(\frac{h_{conv}A}{mC}t\right)}\right] \tag{3.21}$$

This evolution of the temperature could be fitted to an exponential equation of the type:

$$y = a + b\left[1 - e^{-Cx}\right] \tag{3.22}$$

All the parameters are known, so this temperature evolution is used to check the real heating behaviour. Moreover, Equation 3.22 allows to fit the temperature evolution, as shown in Figure 3.11.

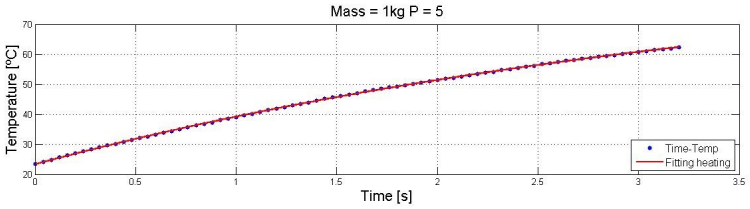

Figure 3.11: Example of a fitting curve in a Heating tests

3.4 Results and discussion

This section explains the results of the tests described in Section 3.3. Following those tests, this section is divided in three parts: the first one describes the parameters calculated from lab tests in order to run the model, the second one the model is run and its behaviour checked. The last part of this chapter is the model validation.

3.4.1 Parameters

Following the steps described in the last section, the parameters obtained from the isothermal and isobaric tests are shown in this subsection. Those parameters have been gotten analysing the data saved with MATLAB®Software. Specific codes were created to analyse and compare the data, obtaining the results.

As it has been explained, the isothermal tests provides the parameters for the model. Every parameters and tests are calculated for SmartFlex®wires from SAES Getters. The SMA wires utilized in this Thesis are wires of 0.4 mm of diameter. The density and specific heat are provided by the manufacturer, and the other parameters are obtained by testing the wire as has been explained previously. A summary of these parameters is shown in Table 3.3.

ρ_{SMA}	$6450 kg/m^3$
C_p	$500 J/kg \cdot K$
$Diameter_{SMA}$	$0.4 mm$
T_L	$363 K$
E_A	$45.1 GPa$
E_M	$41.8 GPa$
σ_L	$409 MPa$
$\Delta\sigma_T$	$8.16 MPa/K$
σ_R	$309 MPa$
ε_T	0.0521

Table 3.3: List of model parameters from isothermal test at $T_L = 363K$ and $T_H = 383K$

Finally, the last parameter gathered is the convective heat transfer coefficient. The temperature decays were measured by the infrared camera, where fitted to Equation 3.17 using OringinPro®. The temperature taken in an account was provided by Line 1 of the temperature, as has been seen in Figure 3.6. The results of the fitting are shown in Table 3.4.

The flow rate gauge utilized was analogic and its the sensitivity is $2 l/min$. Moreover, the airflows values were visually measured. Those tests were done for different weights, from 1kg to 5kg, for each aperture of the valve. As has been described, the aperture of the valve was from 0V

Valve [V]	Airflow [l/min]	y_0	a	R_0	R^2	$h_{conv}[W/m^2K]$
0	0.0	45.22	66.08	-0.36	0.99	116
0.5	1.4	48.13	61.18	-0.40	0.99	128
1	5.9	45.43	65.39	-0.90	0.99	290
1.5	9.1	44.17	70.13	-0.95	0.99	308
2	11.4	45.50	70.33	-1.95	0.99	629
2.5	14.3	45.81	65.56	-2.32	0.99	748
3	16.3	48.64	62.31	-2.43	0.99	783
3.5	18.6	46.89	67.60	-2.64	0.99	851
4	20.8	47.06	62.45	-2.87	0.99	926
4.5	22.6	47.46	66.79	-3.05	0.99	985
5	24.1	47.46	56.38	-2.38	0.99	952

Table 3.4: Measured airflow and fitting results

to 5V. The heat transfer coefficients show an almost linear increasing values versus the airflow, as shown in Figure 3.12. Some values do not follow the linear increasing fit because of a small air leak was detected on the pneumatic junction between the actuator and the pneumatic tubes. The figure illustrates the importance of the active cooling, where can be seen that the maximum h_{conv} is 8.5 times higher than the natural convection. For that reason, the wire behaviour at different flow rates is studied in Chapter 4.

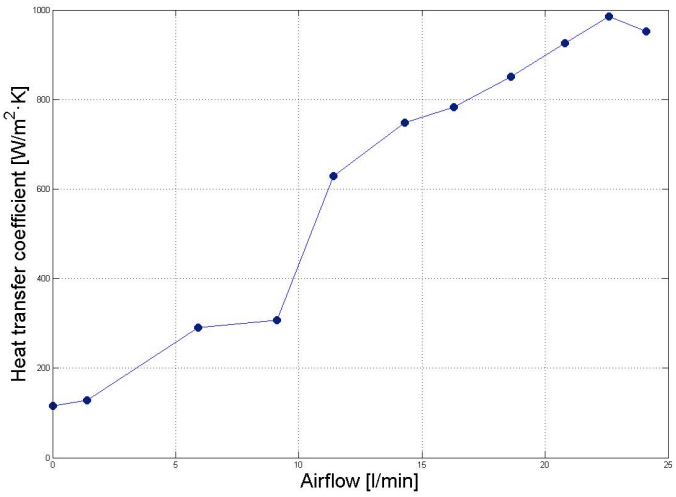

Figure 3.12: Relationship between the heat transfer coefficient and the airflow

Regarding to the heat losses on the system, a thermal study was done. This study determines the influence of each heat loss. As it has been seen, the total thermal resistance depends on the h_{conv}. For each h_{conv} gotten, the thermal resistances were calculated obtaining the influence for each loss. A summary of these resistances is presented in Table 3.5. As expected, the most important heat loss way is the convective heat transfer in the channel with the maximum percentage of the total. The maximum attainable working rate is looked for on the beam actuations, so can be concluded that the convective influence is more 95% of the total thermal resistance. For this reason, the conductive influence in the calculation of the loss heat transfer is ignored, taking the convective transfer the only heat loss.

All the necessary parameters for the model have been described. Also, the convective heat

h_i	R_3	R_3%	R_2	R_2%	R_1	R_1%	Thermal Resistance
116	329.84	6.72%	125.74	17.64%	29.31	75.64%	22.1755
128	328.00	6.27%	125.74	16.35%	26.56	77.38%	20.5590
290	316.79	3.28%	125.74	8.25%	11.72	88.47%	10.3750
308	316.21	3.11%	125.74	7.82%	11.04	89.07%	9.8344
629	311.25	1.64%	125.74	4.05%	5.40	94.31%	5.0987
748	310.45	1.39%	125.74	3.44%	4.54	95.17%	4.3266
851	309.94	1.23%	125.74	3.04%	3.99	95.72%	3.8252
926	309.63	1.14%	125.74	2.81%	3.67	96.06%	3.5276
985	309.42	1.07%	125.74	2.64%	3.45	96.28%	3.3241
952	309.54	1.11%	125.74	2.73%	3.57	96.16%	3.4349

Table 3.5: Results of the total thermal resistance and its influence for each losses way

transfer can be confirmed as the only heat loss ways. These considerations allow to run the model properly, continuing with the validation process.

3.4.2 Simulation

Once the parameters have been obtained, the model can run a simulation. Using the equations described in Section 3.2.1, isothermal simulations were done. A strain control test was implemented for different temperatures as laboratory tests. The Joule influence was not required in isothermal tests, due to any current was not across the wire. The input used has been introduced in Equation 3.4, following:

$$\varepsilon(t) = (strain\_induced) \cdot (tri1 - tri2) \tag{3.23}$$

where $tri1$ and $tri2$ are triangular functions controlled by the maximum strain induced (7%) on a wire of 200mm and seconds per triangle (6.5 seconds). This strain rate is a tuning parameter on the model. The simulations were run at the same temperatures than the lab tests. These temperatures were from 363K to 403K, every 5K, and their results are shown in Appendix A Figure A.2. Same results are illustrated in Figure 3.13.

As Figure 3.13 shows, the curves have apparently good shape and behaviour. The hysteresis loop is going up and lengthening with increasing temperature. This phenomenon has been explained in Figure 2.4b, where depending on the test temperature, phase stresses (austenite and martensite stresses) are different. Therefore, the hysteresis loop lengthens for high temperature (tests above 393K), because austenite and martensite phases are at the same time. These phases show that the transformation is not completed. Those results have to be compared with the experimental tests in order to validate the model.

3.4.3 Validation

In order to validate the model, the data obtained from isothermal experiments in the lab and the corresponding COMSOL simulations have been put together in graphs. These results are shown in Appendix A Figure A.3, and a summary of them in Figure 3.14.

Figure 3.14 shows that the simulations in COMSOL show good agreement with experimental data. There are some inaccuracies in the curvature when phase transformation happens, because the model applied here is a single crystal model, whereas the SMA wire used is polycrystalline. Despite those inaccuracies, the model captures the SMA wire's behaviour well. The parameters described in Figure 3.2 have been compared numerically in experimental and simulation tests. It can be concluded that the maximum stress fits well in most of the cases. The stress hysteresis loop's width is also well captured by the model. Only at high temperatures the model does not predict the maximum stress, its hysteresis loop nor the martensite transformation properly, although the

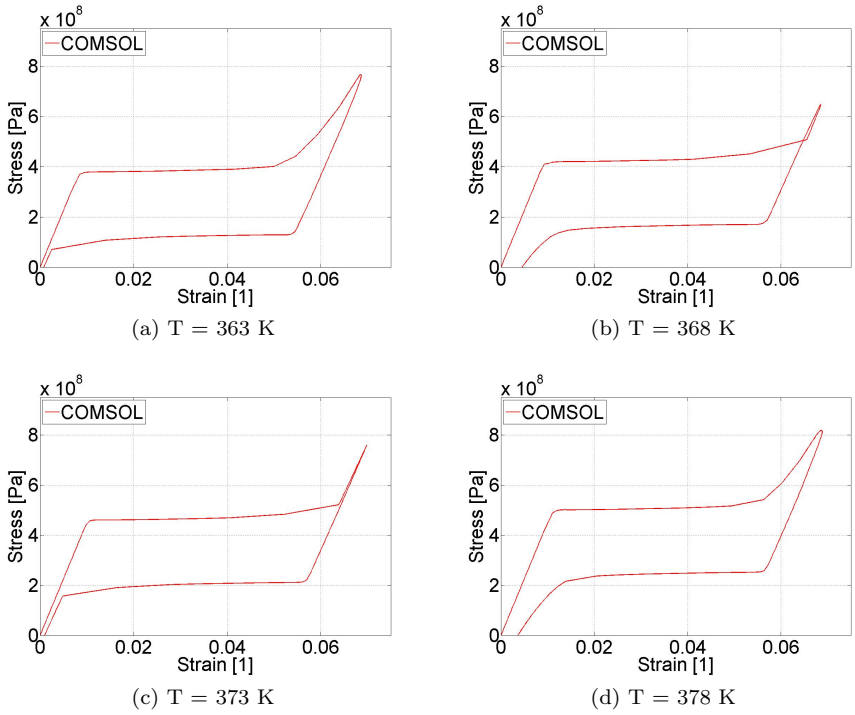

(a) T = 363 K (b) T = 368 K

(c) T = 373 K (d) T = 378 K

Figure 3.13: Isothermal test with COMSOL data

curves follow its behaviour. For all these reasons, the isothermal test is demonstrated and validated with the model described, being able to show the SMA behaviour at different situations.

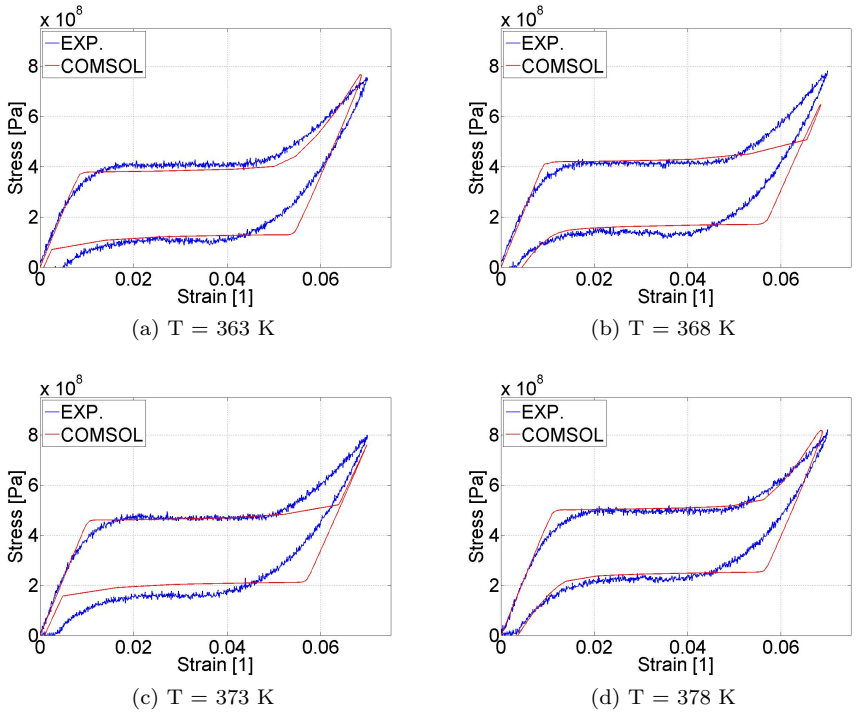

(a) T = 363 K (b) T = 368 K

(c) T = 373 K (d) T = 378 K

Figure 3.14: Validation of isothermal test, comparing laboratory and COMSOL data

3.5 Conclusions

Before the validation of the model, some important points have been demonstrated. One of those aspects is that the model requires some parameters in order to be run. These parameters can be obtained in an easy way by means of two different isothermal tests and isobaric tests. The isothermal tests provide the parameters analysing the SMA curves, as a geometrical parameters. On the other hand, the isobaric tests allows to calculate the convective heat transfer coefficient, which has been obtained analysing the cooling process on the wire. Moreover, this heat transfer has been confirmed as the only heat loss in the system, as seen after the thermal study done.

All of those conclusions allow to run the model successfully. After comparing the results with the experimental tests, the model has been validated. The model shows a good agreement with the results obtained by experiments. The compared parameters demonstrates that the model fits properly for different temperatures, being able to be used for different kind of tests and situations.

Chapter 4

Working rate for a SMA: experimental and simulation comparation

Once the SMA wire's model has been described and validated, the process that occurs in the isobaric tests is analysed. This chapter provides a better understanding of the cooling and heating process. Thus, the validated model is used to compare the results with the experimental tests during the cooling and heating. Finally the maximum attainable working rate is obtained in both cases (experimental and simulation), comparing the cooling and heating results at the same time. Moreover, the attainable frequency on the wire used in this Thesis is found, using different strain-ratios and references from the full strain range.

4.1 Introduction

This section explains in detail the isobaric tests, studying the processes and their influences on the wire: cooling and heating. As it has been explained in Chapter 3, the isobaric tests are experiments in which the wire is tested with temperature variations under a constant load. These temperature changes are possible modifying by the current across the wire (Joule heating). Once the model has been validated, the model is used in those kind of tests.

The goal of this section is to find the maximum attainable working rate on a single SMA wire. This working rate is calculated under different cooling-heating rates and load conditions. Thus, the model is used to predict this working rate, comparing the simulations with the experimental results. In order to be able to get those comparisons, the same inputs were implemented in the lab and software, simulating the same tests.

Before achieving the working rate, a better understanding was necessary in cooling and heating process, analysing two different parts of the isothermal tests: cooling test and heating test. These tests were done for different weights, from 1kg to 6kg. A schematic configuration is shown in Figure 3.4. Once the tests were done, the results were compared with the simulations in COMSOL, being able to obtain the working rate on the wire. Those cooling and heating tests are explained in Section 4.2, as well as the process to get the attainable frequency on the wire.

Finally, another kind of tests are studied in this chapter. The tests consisted of working on different areas of the full strain range. Those strain-ratios provide different attainable frequencies depending on the working strains. Those tests were not implemented in COMSOL, only experimental results.

4.2 Methods and experimental

In this section, the tests described previously are explained in detail and also how the study has been done. As it has been aforesaid, isobaric tests were implemented according to Figure 3.4. The tests were done for different weights, from 1kg to 6kg. Different cooling and heating rates were applied for each weight. Those tests are explained in Subsection 4.2.1 and Subsection 4.2.2 respectively. A consequence of those studies is the working rate of the actuator. Their results can be compared in order to get the maximum working rate, one of the goals of this chapter (Section 4.3). Also, specific tests for the attainable frequency are explained in Subsection 4.2.3, analysing its influence and actuation responses depending on the chosen strain reference.

4.2.1 Cooling test

In this test, the goal is to understand the influence of the cooling, one of most important features of this actuator. Different cooling rates were analysed, ignoring the heating process. As has been explained in Section 3.3.2, the wire was heated up keeping constant power that heated the wire over T_{Af} what guaranteed that the SMA tested complete its transformation into austenite. Subsequently, the current was cut off at the same time that the valve was opened, cooling the wire with different flowrates for each weight. A timing diagram with inputs (Joule and valve aperture) and expected outputs (temperature and strain) is shown in Figure 3.7. These tests captured the wire behaviour during cooling, providing the recovering time for different inputs (weights and flowrates) and the convective heat transfer coefficient (h_{conv}) for every flowrate. With the h_{conv} from the previous chapter, the times that the wire takes to recover to its memorized shape were calculated.

In order to determine those times, the tests were done following the configuration described in Chapter 3. The data saved was analysed with MATLAB. Those experiments were done for different weights, from 1kg to 6kg in steps of 1kg, and flowrates. The flowrates depended on the aperture of the valve, which was from 0V to 5V in steps of 0.5V. The number of the experiments was 66. One of them is shown in Figure 4.1.

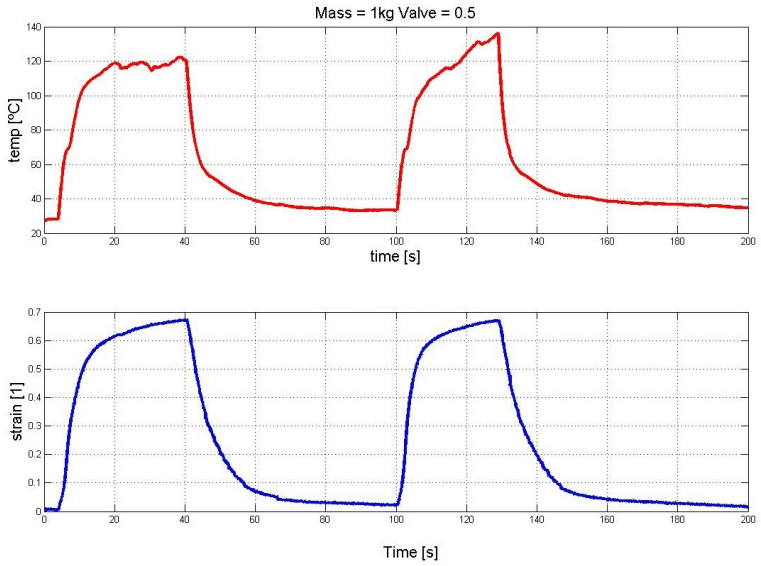

Figure 4.1: Timing diagram with laboratory data in Cooling tests

In the Figure 4.1, the evolution of the temperature and strain can be seen in a test run to 1kg and 0.5V of the valve aperture. Two complete cycles were done, allowing to analyse the recovery

time for the cycle with the maximum decay. A MATLAB script was written to find the maximum slope, taking the best cooling cycle in the recovery time, as Figure 4.2 shown at the same test.

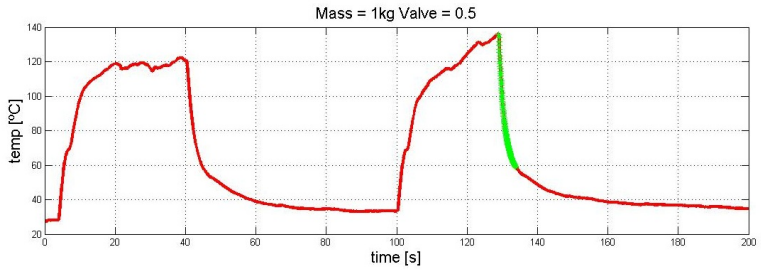

Figure 4.2: Temperature diagram with the maximum decay detected

Once the maximum temperature decay was detected, it was located in the strain time series. This is like that because the temperature is unstable and does not take a constant value to determine a rate for all the tests. The strain has not strong variations during the cycle, as it is shown in Figure 4.1. Therefore, a manually rate was determined in the strain time series in order to get the time that takes for the wire to recover its shape. In this test, the rate was optimized to 10% and 90% of the full strain range, locating these points on the timing diagram. Figure 4.3 shown those points in the strain plot.

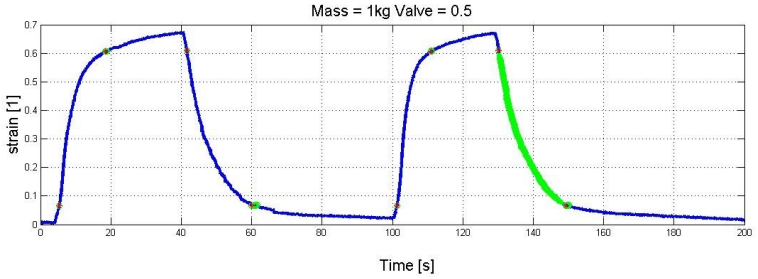

Figure 4.3: Strain diagram with the maximum decay detected

Those strain points were carried forward to the temperature at the same time point, calculating thus the recovery time (cooling time), as can be seen in Figure 4.4. These process were done in a iterative code, allowing to obtain the recovery time for all the experiments. These results are shown in Section 4.3.

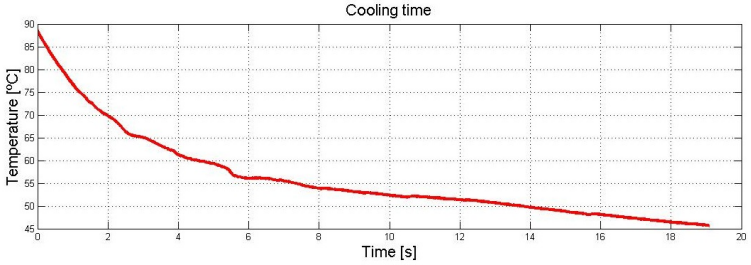

Figure 4.4: Recovery time in temperature diagram

4.2.2 Heating test

Similar tests were done in this section. Now the heating process was studied, seeing its influence on the SMA wire. The inputs were different, keeping constant the airflow on the wire. The aperture of the valve was completely opened, being the airflow at its maximum. This is due to the cooling process was not interesting now and the transformation into martensite was faster. Also in this test, the airflow was cut off at the same time that the power supply was turned on, heating the wire with different powers for each weight. A timing diagram with the new inputs (Joule and valve aperture) and expected outputs (temperature and strain) is shown in Figure 4.5. With those tests, the heating behaviour on the wire was analysed, obtaining the time that takes for the wire to be contracted.

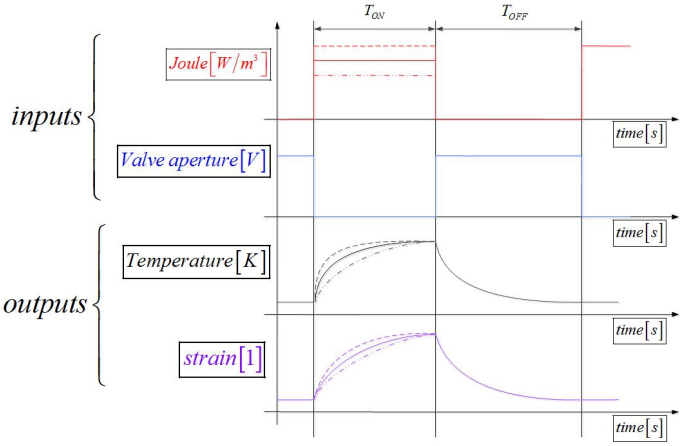

Figure 4.5: Input signals and expected outputs in heating tests

The cooling setup and method were utilized during these tests, as has been described in Subsection 4.2.1. Thus, weights from 1kg to 6kg were tested for different powers. Those powers were determined manually, taking the minimum power as the power need to reach the austenite phase completely, and the maximum power as the maximum capacity of the power supply. In summary, the power was going from 5W to 40W, every 5W. One of those experiments is shown in Figure 4.6. The maximum rise of the cycle was also detected, guarantying the best slope to calculate the heating time. For the same reason than the Cooling tests, this slope was carried forward to the strain diagram due to its constant behaviour. This strain is also illustrated in Figure 4.6.

The transformation time from the martensite into austenite was obtained in a iterative process. Those times were calculated in MATLAB using a specific ratio. This ratio was optimized to 10% and 90% of the full strain range, as it was done in Cooling tests. These results are shown in Subsection 4.3.2.

4.2.3 Attainable frequency on a wire

Following the isobaric tests described previously, a better understanding of the maximum attainable frequency on a wire was required. These tests allow to know the working frequencies for different situations depending on the full strain range. The power (40W) and the airflow (5V) were applied now, making the wire work with a limitation of the strain range. Thus, the goal of the test was to calculate the attainable frequency on a wire relaying on what strain is to be recovered. This strain-ratio was determined by the relationship between the amplitude peak to peak that was studied and the full strain range. Thus, this strain-ratio was from 5% to 100% of the full strain range. Moreover, three different tests were done. Those tests depended on the strain reference taken. That is, the tests were done from the maximum, minimum, and midpoint

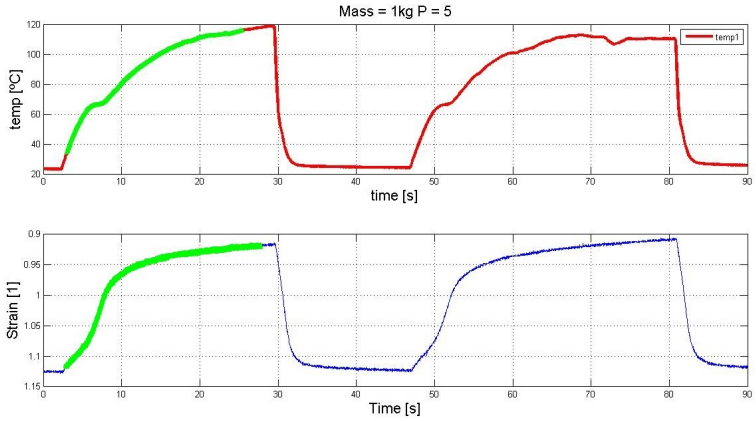

Figure 4.6: Timing diagram with laboratory data in Heating tests, including the heating time.

of the strain. A schema about how this test was implemented is shown in Figure 4.7.

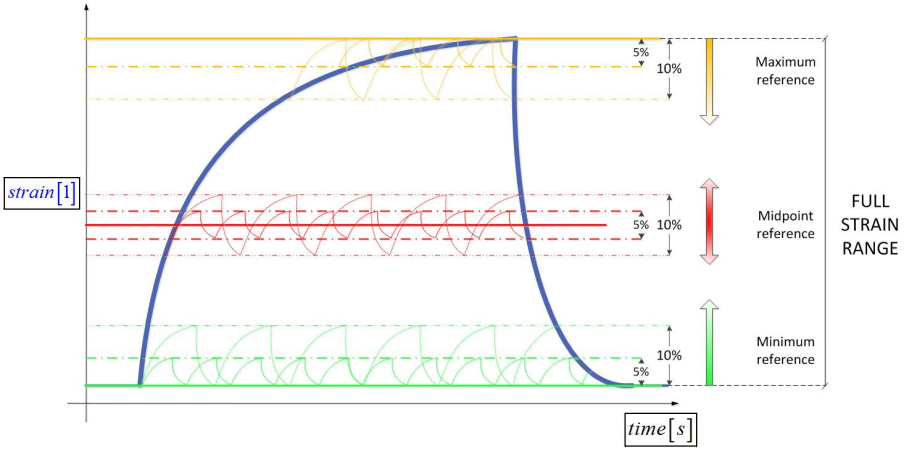

Figure 4.7: Schema of the attainable frequency study

Those tests were able to analyse the attainable frequency for different references. Those references were compared between them for the same weight. The tests were done for 1kg load. The maximum strain peaks were found in the graphs, calculating the time that takes for a wire cycle. Thus, its frequency could be obtained. Also, those tests were repeated during some cycles to achieve the average of the results, minimizing the inaccuracies produced in a single cycle.

In order to be able to analyse these tests, the same tests were also done in a thinner wire and different weights. The used wire was 0.2mm of diameter. In order to make the results comparable, the first wire (0.4 mm of diameter) was tested for 1 and 2 kg, and the second one (0.2 mm of diameter) for 0.25 and 0.5 kg.

Moreover, the wire used in this Thesis (0.4mm of diameter) was thermally analysed, checking its behaviour. This test was done only for 1kg load with different references. Thus, the relationship between the temperature and the strain could be studied. Comparing the strain - temperature at the same reference (maximum, minimum or midpoint), the attainable frequency was analysed within the loop. This provided what the strain - ratio influence was in the system, knowing how the SMA wire was working for each reference and its influence area.

4.3 Results and discussion

The results of the tests are shown in this section. Following the sequence explained in Section 4.2, the cooling and heating tests results are detailed. Comparing their results, the maximum working rate can be found for the wire. Both tests have been implemented in COMSOL and the cooling and heating times have obtained as well as the simulation working rate. After that, the maximum attainable frequency is gotten and compared for different wires, aside from the thermal influence in a specific weight for each reference.

4.3.1 Cooling tests

As it has been described in Subsection 4.2.1, the isothermal tests were implemented in COMSOL with the same input. Different weights and airflows were simulated following that section. The tested weights were from 1kg to 6kg with the convective heat transfer coefficients obtained in Subsection 3.4.1. One of the experiments is shown in Figure 4.8, where the temperature and strain evolution can be seen.

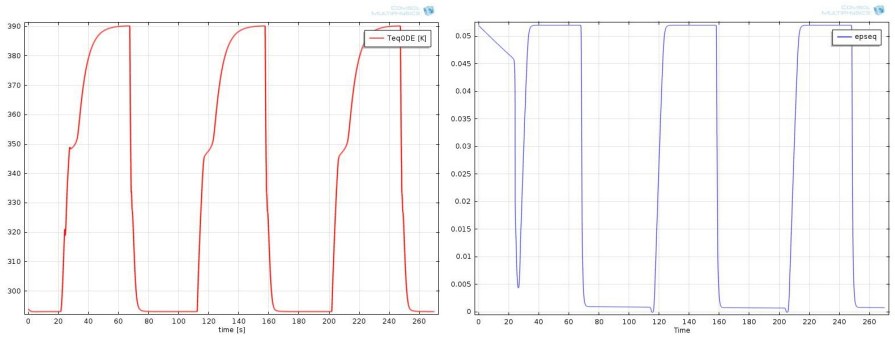

Figure 4.8: Timing diagram with COMSOL data (temperature and strain) in Cooling tests

In the simulation case, all the cycles follow the same evolution and, therefore, the maximum slope in the temperature diagram is not detected. Thus, the recovery time was calculated directly from the strain diagram. For that reason, the recovery time is calculated with the same ratio than the experimental tests, from the 10% to the 90% of its maximum strain. Figure 4.9 shows the calculation of the recovery time.

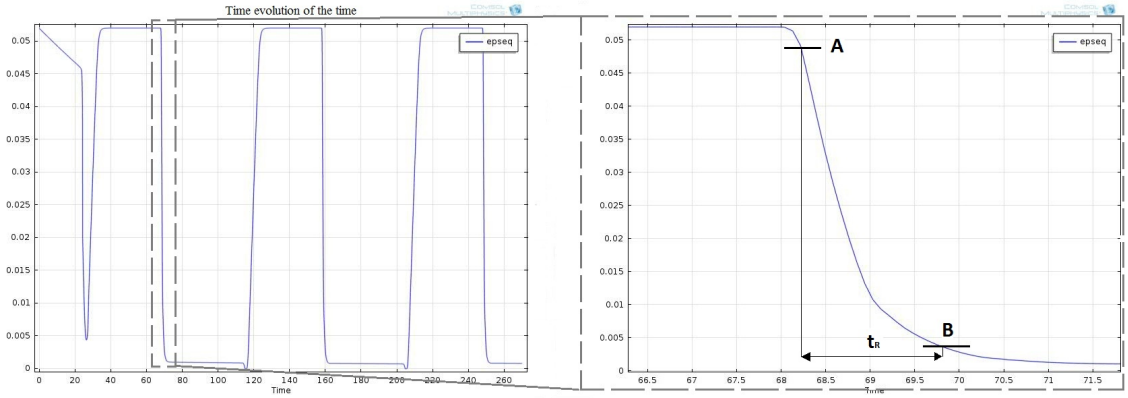

Figure 4.9: Recovery time in strain diagram with COMSOL data

Obtained those times in COMSOL, the experimental and simulation recovery times can be compared. A summary of the experimental and simulated recovery times for different loads is

shown in Figure 4.10. Some simulation problems were appreciated for high loads, because the software could not converge in a solution. For that reason, only data from 1, 2 and 3kg were calculated.

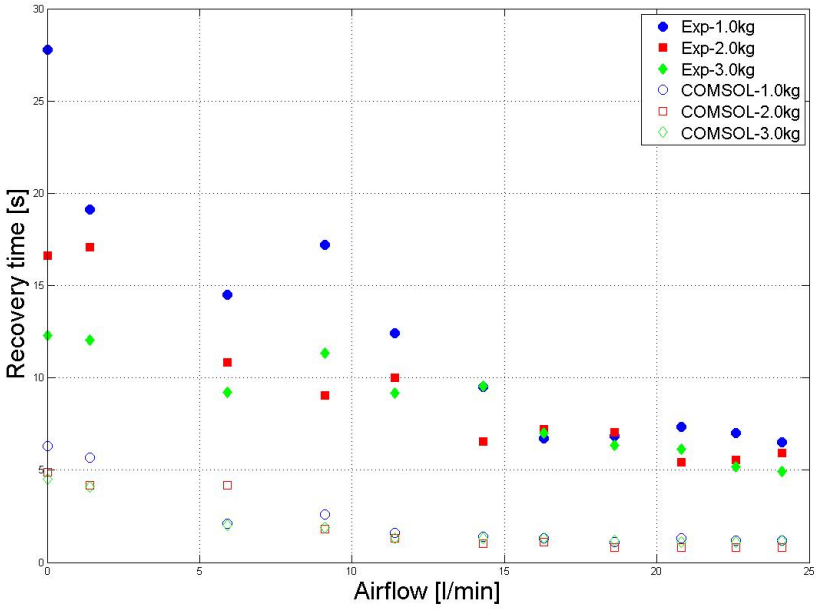

Figure 4.10: Recovery times for model simulations and experimental tests

As Figure 4.10 shows, some inaccuracies are appreciated between the COMSOL model and the experimental data, but with a similar behaviour. In both cases, recovery time for small valve apertures are much longer than those at high airflows, as expected. Furthermore, from a certain value of the airflow, increasing the airflow does not have a significant consequence on the recovery time because the time is limited by the time that it takes for the austenite phase to be transformed into martensite. In addition, it can be observed that the heavier weight contribute in the recovery time for the same airflow, because the applied load cooperate with the cooling process, contributing to its elongation.

The disagreement can be explained by comparing the behaviour of the model and the SMA wire for an isobaric test. As shown in Figure 4.11, the temperature's hysteresis loop are different in both cases, being overall the transformation temperature from austenite to martensite smaller in simulation data than the experimental data. Due to this, the recovery times from the simulations are shorter than from the experiments. Regarding the strain, a difference between the maximum recoverable strain is appreciated in experimental data, being always smaller than the simulation strain. This is because the COMSOL software has been implemented for a single crystal model, whereas the tested SMA wire is polycrystalline. The crystallinity on the wire controls the direction in which the contraction happens. Therefore, a single crystal wire is contracted in only one direction whereas a polycrystalline wire is contracted on random directions, being the transformation times shorter in the simulations.

4.3.2 Heating tests

Those heating tests has been developed in COMSOL as well. The inputs were implemented following the experimental tests, where the power chosen and the maximum airflow worked alternatively. Those simulations were done from 5W to 40W for different weights, and one of them is shown in Figure 4.12. As it can be seen in the figure, the temperature takes high values until it is stabilized.

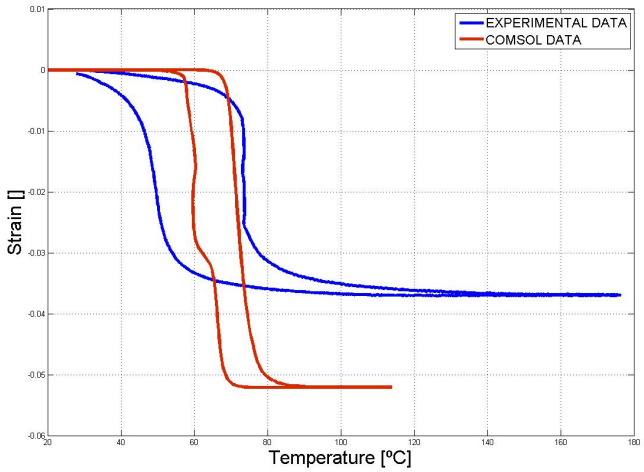

Figure 4.11: Model and experimental results for an isobaric experiment at T = 263K with a mass of 1.25 kg

Mathematically, this result is correct using the equations described, because no temperature limits were defined in terms of any conditions. Those high temperatures do not take on importance to the strain due to the strain is constant when the wire recover its memorized shape, being able to analyse the heating time on the strain diagram.

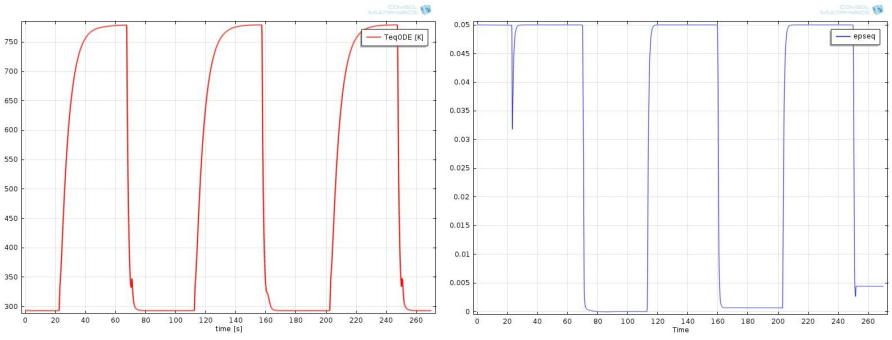

Figure 4.12: Timing diagram with COMSOL data in Heating tests

Analysing the strain diagram, the heating time was calculated. This time was done using the same heat rate than the experimental tests, optimized as a 10% of the strain limits. Therefore, the COMSOL data have been imported and analysed in MATLAB, and the heating times have been obtained in a iterative process from different weights. Those results are able to be compared with the experimental times.

The experimental and simulation times were collected and compared for different weights. A summary of the heating times for both tests is shown in Figure 4.13.

As can be seen, the times show a good behaviour and similar than the real experiments. Some inaccuracies are appreciated between the COMSOL data and the experimental data, mainly during the first values of the power. In both cases, and more noticeable on the experimental data, the time that it takes for the wire to be heated decreases for higher powers applied. Those values are stabilized from 30W, being the time difference of the order of hundredths of a second. Moreover, the weights are not decisive in this tests what means the heating times in a determined power are practically the same for different weights, except to small powers in experimental data. The

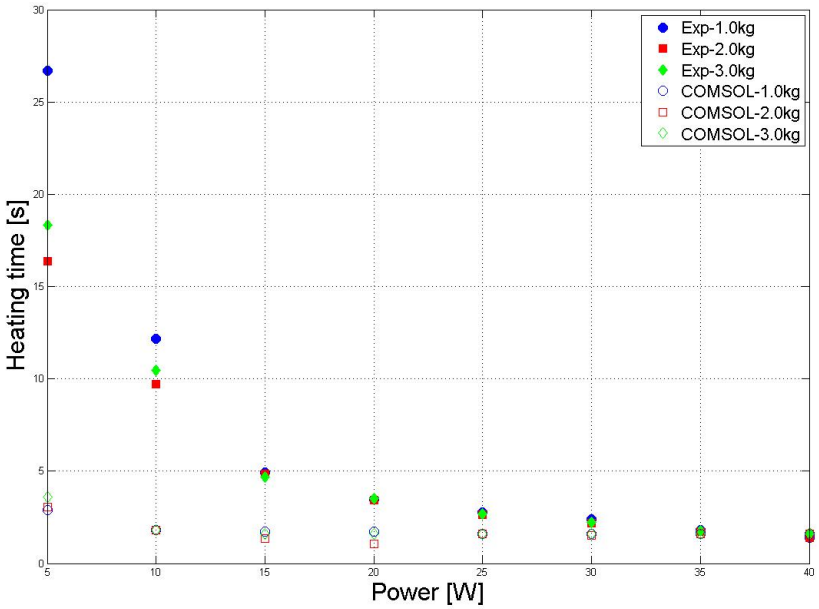

Figure 4.13: Heating timess for model simulations and experimental data

reason can be found in the timing diagram, where the transformation into austenite takes more time. Another reason is that the laboratory conditions could be modified.

The disagreement can be explained for the model used. As been seen in the previous subsection, the COMSOL model implemented is a single crystal model, whereas the tested SMA wire is polycrystalline, where the contraction can be possible on a unidirectional way or random directions, depending on the orientation of the grains. Moreover, those inaccuracies can be seen in Figure 4.14, where the timing diagram of the temperature and strain have been compared in a specific test. That is possible because both tests have been implemented with the same inputs. In the Figure, the strain diagram shows that during the heating, the experimental curve is smoother in the start and in the end than the simulation curve, whereas both curves have the same slope between those points. Thus, the heating time is shorter in a simulation tests due to the transition time in the extreme points.

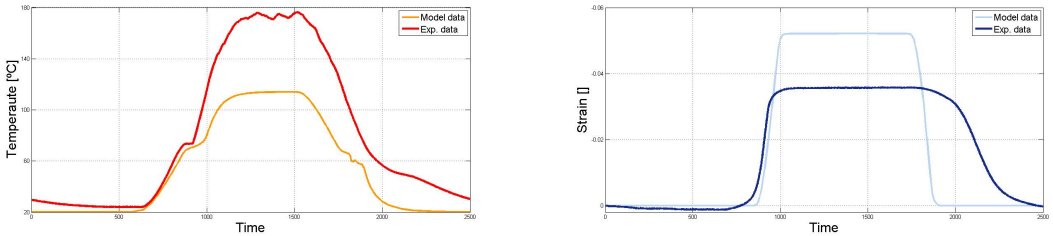

(a) Temperature diagram

(b) Strain diagram

Figure 4.14: Model and experimental timing diagram for a isobaric experiment at $T = 263K$ with a mass of $1.25kg$

4.3.3 Working rate

Once the cooling and heating tests have been done, the results can be compared achieving the working rate on a wire. Those tests provided the recovery and heating times to different situations, where the airflow and power are the inputs for each test. Comparing the time that it takes for the wire to be elongated and contracted, the maximum working rate of the wire is calculated. Those rates have been gotten for the experimental and simulation data. A summary with all the weights for model and experimental data is in Appendix B, and Figure 4.15 shows this working rate for 1 kg.

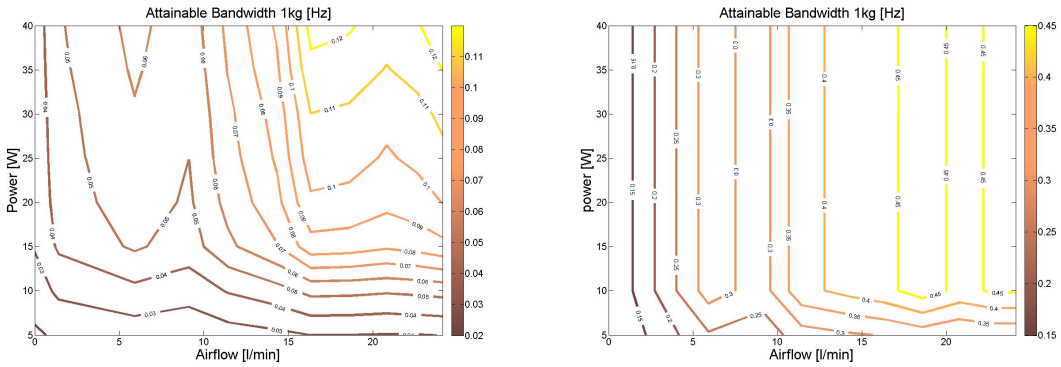

(a) Experimental data

(b) Model data

Figure 4.15: Experimental and model attainable working rates (in Hertz) with a load of 1 kg

As it can be seen in the Figure, the working rates are not similar in the model and the experimental test. For the reasons explained previously, the SMA wire's model has faster responses than the actual wire, but the tendency is similar. The graphs show higher working rates for higher powers and airflows, but limited for both inputs. For low working rates, the limiting factor is the power input to the system, and for higher working rates is the airflow.

4.3.4 Attainable frequency on a wire

The maximum attainable frequency for different references was obtained and compared. Figure 4.16 shows the results of the test for 1kg.

As it can be seen in the Figure, the attainable frequency is higher for lower strain-ratios. Comparing them, this frequency is also maximum for the midpoint reference. This is due to the transformation of martensite into austenite or vice versa happens between the extremes points. Thus, the midpoint reference has the fastest actuation responses. This frequency is closely followed by the maximum reference. In this case, its responses are a little bit slower for smaller strain-ratios. Exceeded the first strain-ratios (until 50% of strain-ratios), its responses can be compared with the midpoint reference. Regarding the frequency from the minimum reference, its responses are the slowest as was expected. In this case, the reference is the minimum strain point. This point is at room temperature, because the maximum elongation happens when the wire is cooled. For that reason, the active cooling is the determining factor taking the longest responses. Finally, all of the cases have a close response for the maximum strain-ratio (100% of the strain-ratio), because they are working on the same strain area.

Figure 4.17 shows the comparison between these results of the different wires and weights. In this figure, only the midpoint reference is illustrated because it shows the last results. As it can be seen in the Figure, the stress is not a decisive factor on the system. Comparing the results for the same wire, the actuation responses are really close. Regarding to the behaviour for different wires, the diameter influence is noticeable. Faster responses are found in the thinnest wire due to the

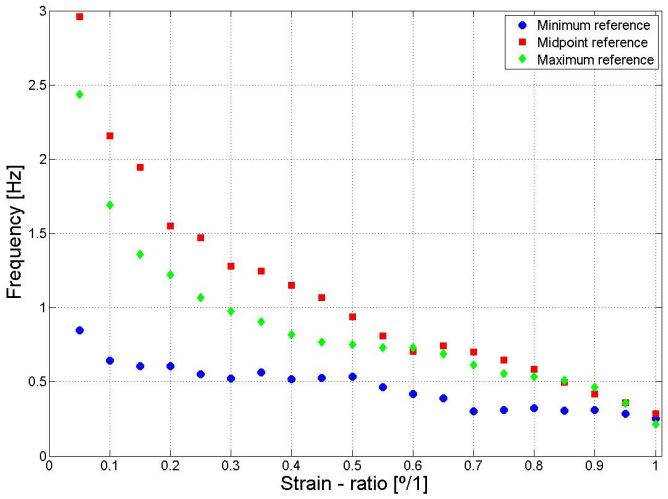

Figure 4.16: Maximum frequency attrainable for different references

cooling influence. For smaller diameters, it takes for the wire less time to be at room temperature getting the transformation into martensite faster, and consequently higher actuation frequencies.

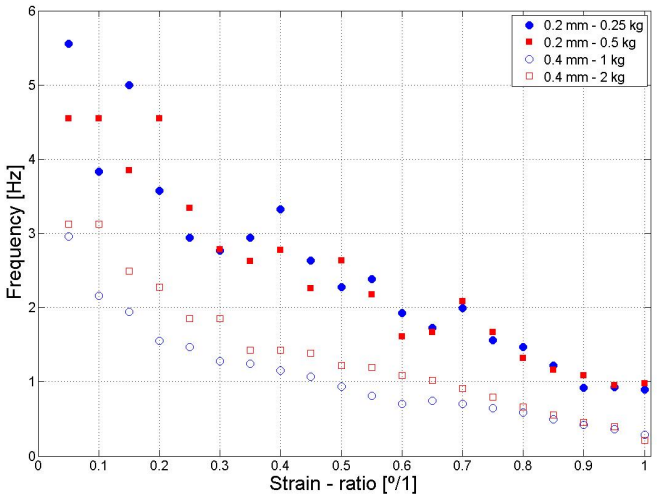

Figure 4.17: Maximum frequency attrainable for different weights and wires in a midpoint reference.

Moreover, the strain - temperature can be compared for the same reference (maximum, minimum or midpoint). As has been explained, the attainable frequency can be analysed inside the temperature - strain loop. This provides what the strain - ratio influence is on the system, knowing how the SMA wire is working for each reference and its influence area. Figure 4.18 shows the influence is for each test, marking in a red line the working rate for the maximum strain - rate (100% of the strain).

As it can be seen in the figure, different behaviours and influence areas are appreciated depending on the reference point. Analysing each graph separately, some conclusions can be shown: Figure 4.18a shows the lowest working temperatures, closer to the room temperature. This means

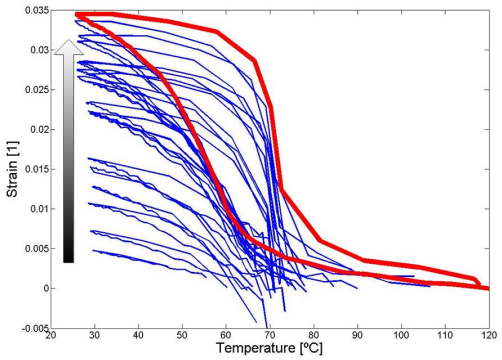

(a) Minimum reference

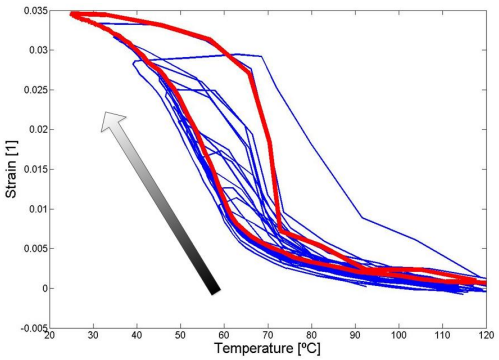

(b) Maximum reference

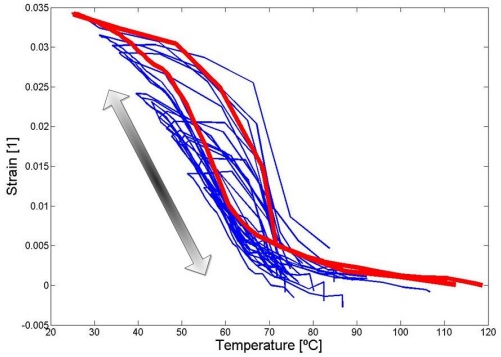

(c) Midpoint reference

Figure 4.18: Thermal influence for working rates with a mass of 1 kg

that the wire is working in most of the cases into martensite phase and takes working rates longer. The opposite case is shown in Figure 4.18b, due to the wire is working in most of the cases into austenite phase. This means that the wire operates at higher temperatures where the cooling influence is more significant. A intermediate behaviour is shown in the midpoint reference (Figure 4.18c), where the wire is working from a mix phase to complete transformation martensite into austenite. Therefore, the midpoint reference takes faster actuations responses, as it has been explained previously.

4.4 Conclusions

Some aspects have been demonstrated in this chapter. The determinant inputs on the system are the power and the airflow. Testing a wire for different inputs, the heating and cooling responses have been analysed. Those times were obtained for different weights, comparing them with the simulation data. The combination of the heating and the recovery times allowed to get the time that takes for the wire to complete one cycle. Thus, this overall time was used to calculate the maximum working rate for each combination of input power and airflow along the wire. This actuation frequency is limited by the power and airflow in experimental and simulation tests. The model has faster response mainly due to the model chosen. The model implemented was a single crystal wire. That means the contraction happens only in one direction, whereas the real wire has it on random directions (polycrystalline).

Moreover, the best strain to test the wire is around the midpoint. This reference showed a faster actuation responses due to the transformation phases happens in the middle of the full

strain range. This attainable frequency is almost 3.5 times higher at the midpoint reference that the minimum reference for same conditions of power and airflow. The better responses were also checked in a thermal study, where the temperature influence could be analysed. Another important point is that this attainable frequency does not depend on the load applied. The same actuation responses were observed by comparing the results for different weights. Higher frequencies were obtained for a thinner wires. In those wires, the active cooling was the determining parameter achieving faster cooling times.

Chapter 5

Model validation for antagonistic set up

Once the model has been validated for a single wire, this chapter is focused on the model validation for antagonistic setup. This model is a continuation of the model described in Chapter 3, and the same steps are followed here in order to get the model. Thus, this chapter describe the model obtained, its equations and the its parameters. Moreover, those parameters are explained as well as the process followed to get them. Finally, the experimental data and simulation data are compared, looking for the validation of the model.

5.1 Introduction

After the SMA wire's behaviour has been modelled and validated, the antagonistic setup was implemented. The goal of this chapter is to study the behaviour of the actuator. Two wires were embedded on the actuator, where the channels are above and under the neutral axis. In this configurations, two different lines of wires were on the beam, allowing its deflection on both directions when the wires in each side are contracted. This deflection modifies the geometry of the trailing edge, being able to be adapted to the current flight conditions. Figure 5.1 shows the actuator clamped on a flap frame on the trailing edge, where the deflection can be observed.

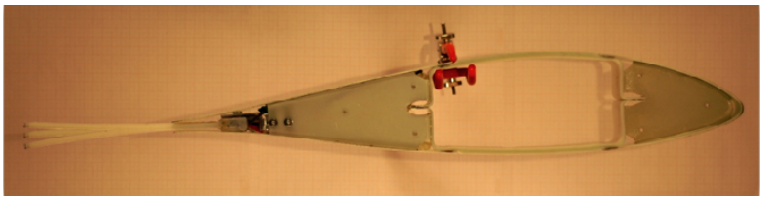

Figure 5.1: Model of the wing profile with the actuator on the trailing edge

Following the single wire described in Chapter 3, the Müller - Achenbach - Seelecke model was used [4, 18]. This model was implemented in an antagonistic setup, as Veeramani et al. explains in [23]. The antagonistic model is detailed in this chapter, as well as the necessary parameters in order to run the model. Finally, the model is compared with the experimental results and the model validation is obtained.

5.2 Theory model

The Müller-Achenbach-Seelecke model was implemented in an antagonistic setup, where two wires were embedded on an actuator. The bending actuator mechanics were described using a "circular arc bending model", which has been developed by Veeramani et al. [23]. Comparing the antagonistic model with the single wire model, two new variables were introduced: the bending angle (θ) and the radius of the curvature (r). In order to describe the antagonistic model completely, first one-SMA beam (one SMA wire and actuator influence) is explained in detail, to reach after that a two-SMA beam (two SMA wires and actuator influence).

5.2.1 Single beam: one-SMA wire and actuator influence

The deflection is produced by the contraction of the wires that are out the neutral axis. During the contraction, the wire creates a moment in the actuator, bending it. The moment applied is related to a tendon stress by Equation 5.1.

$$M = aP_{SMA} = aA_{SMA}\sigma_{SMA} \tag{5.1}$$

where P_{SMA} is the force produced by the SMA actuator, a is its offset from the neutral axis of the actuator, and σ_{SMA} is its stress. The two variable are related now, defining the bending angle as a function of the radius of the curvature

$$\theta = \frac{L_0}{r} \tag{5.2}$$

where L_0 is the length of the actuator, and r the radius of the curvature. This radius is defined as a function of the applied moment on a beam

$$r = \frac{E_{act}I_{act}}{M} \tag{5.3}$$

Combining Equation 5.1 and Equation 5.3, the bending angle becomes

$$\theta = \frac{aA_{SMA}L_0\sigma_{SMA}}{E_{act}I_{act}} \tag{5.4}$$

This bending angle can be defined geometrically with the distance between the wire and neutral axis. Therefore, this new bending angle is

$$\theta = \frac{\Delta L}{a} \tag{5.5}$$

where ΔL is the change in the length of the SMA wire, comparing the pre-strain with the real strain along the time. Thus, ΔL is defined as

$$\Delta L = (\varepsilon_p - \varepsilon(t))\, L_0 \tag{5.6}$$

Equation 5.4, Equation 5.5 and Equation 5.6 are combined, obtaining thus the stress-strain relationship for a SMA actuator attached to a beam:

$$\sigma_{SMA} = \frac{E_{act}I_{act}}{a^2 A_{SMA}} (\varepsilon_p - \varepsilon(t)) \tag{5.7}$$

This equation converts the bending problem into a one-dimensional problem, following the single wire behaviour described in Chapter 3. A schema of the actuator with a SMA wire in parallel with the beam influence is illustrated in Figure 5.2.

As it can be seen in the figure, the actuator stiffness influence has been represented as a spring, due to the similarity of Equation 5.7 with a spring behaviour. Thus, the effective spring stiffness is given by Equation 5.8.

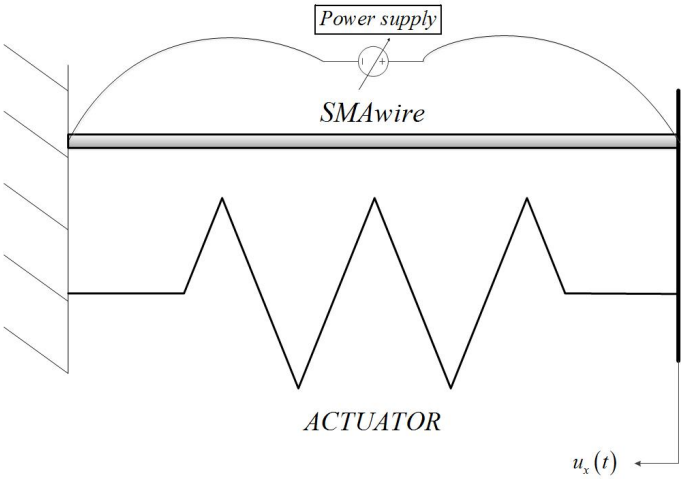

Figure 5.2: Schema for a single beam

$$K_{SMA} = \frac{E_{act} I_{act}}{a^2 A_{SMA}} \tag{5.8}$$

Equation 5.7 is introduced into the single wire model. Thus, this new stress-strain relationship is given by

$$\tilde{\sigma}(t) = \frac{\varepsilon(t) - \varepsilon_T \left(x_{M+}(t) - x_{M-}(t)\right)}{\frac{1-x_{M+}(t)-x_{M-}(t)}{E_A} + \frac{x_{M-}(t)+x_{M+}(t)}{E_M}} - K_{SMA}\left(\varepsilon_p - \varepsilon(t)\right) \tag{5.9}$$

Equation 5.9 represents the evolution of the stress including the actuator influence. This equation is used to implement the antagonistic beam with two wires embedded in the channels.

5.2.2 Antagonistic beam: two SMA wires and actuator influence

Following the single beam model, an antagonistic model has been developed as one-dimensional geometry. This model includes two SMA wires, one in parallel and the other in series with a linear spring (beam behaviour). A schema with this configuration is illustrated in Figure 5.3.

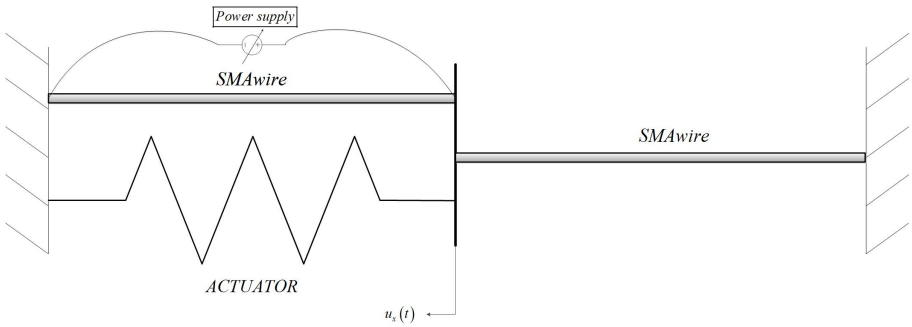

Figure 5.3: Schema for anagonistic beam

In this configuration, two different wires can be seen an active wire and a passive wire. Each wire has its own behaviour, and the beam influence is implemented only in one of them because takes into account the influence of the whole beam. As it can be seen in Figure 5.3, the first wire is the active one with the beam influence. This wire is heated by Joule effect, following the system

of the equations 3.7. The evolution of its stress is given by Equation 5.9. On the other hand, the passive wire is controlled by the strain that provides the active wire. Therefore, its behaviour is like a wire in an isothermal tests, and its stress evolution is given by Equation 3.5.

The equations described in this section explains the SMA behaviour in an antagonistic configuration. The beam influence is included in the model. Moreover, the model can predict the deflection on the actuator, being able to compare those results with the experimental data.

5.2.3 Implementation in COMSOL

The antagonistic model was implemented in COMSOL, following the model described for a single wire. Thus, this model contains dual one-dimensional geometries developed in a two different models in the software, carrying one of the outputs in the first model as a input in the second model. As it has been described in the antagonistic configuration, while one of the wires in the actuator is heated (active wire), the other one is cooled and can be considered a passive wire. For that reason, the COMSOL model uses two different models in its implementation. Thus, the active wire (the heated wire) has the same behaviour that the single beam (Subsection 5.2.1), where the input is the power and the main output is the strain, which is carried out to the next model. The passive wire is similar to a wire tested in isothermal conditions, where the input is the strain which is brought from the first model. Summarizing the antagonistic beam model, the only different variable is the flux term (Equation 3.12), being different in both models, and the boundary conditions. An antagonistic schema for each model and their own geometry is shown in Figure 5.4.

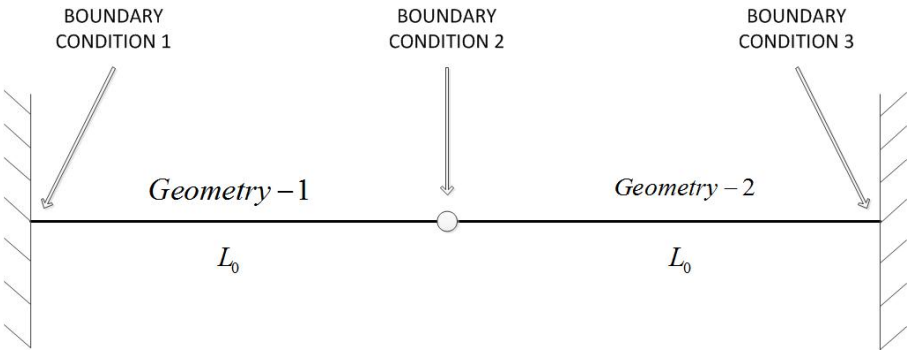

Figure 5.4: Schema of the Boundary Condition for antagonistic beam

The flux term in Geometry 1 is the same than the single beam stress, relating the equivalent stiffness of the flexible actuator to the SMA constitutive model:

$$\tilde{\sigma}(t) = \frac{\varepsilon(t) - \varepsilon_T\left(x_{M+}(t) - x_{M-}(t)\right)}{\frac{1-x_{M+}(t)-x_{M-}(t)}{E_A} + \frac{x_{M-}(t)+x_{M+}(t)}{E_M}} - K_{SMA}\left(\varepsilon_p - \varepsilon(t)\right) \tag{5.10}$$

And this term for Geometry 2 is the same than the stress for a single wire, given by:

$$\sigma(t) = \frac{\varepsilon(t) - \varepsilon_T\left(x_{M+}(t) - x_{M-}(t)\right)}{\frac{1-x_{M+}(t)-x_{M-}(t)}{E_A} + \frac{x_{M-}(t)+x_{M+}(t)}{E_M}} \tag{5.11}$$

As it can been seen in Figure 5.4, three different boundary conditions were defined in order to run the simulation successfully. Some of them were similar to those in the single model described previously and common for both of those models, such as the adiabatic thermal boundary conditions on the clamps and the no boundary conditions in the phase fractions. However another conditions are different and specific for each model. Moreover, boundary conditions in antagonistic setup are different for each geometry. Those conditions for Geometry 1 are:

- The condition at Boundary 1 is fixed. In other words, the displacement is set to zero: $u(0) = 0$.
- At Boundary 2, the displacement is obtained at the fix end of the first geometry. Depends on the temperature on the wire (power input), defining thus the evolution of the strain. This strain is carried out to Geometry 2.
- The initial conditions for the phase fractions are defined in this geometry, where the pre-strain has been done on the wire to embed it on the actuator. Therefore, Geometry 1 is completely in austenite phase.

The boundary conditions defined for Geometry 2 are:

- The condition at Boundary 2 is brought from the Geometry 1, where the input for this model is the strain generated by the first model.
- At Boundary 3, the last point of the model is fixed as well. Its displacement is set to zero ($u(0) = 0$) in a relative coordinates focused on the Geometry 2, or the displacement is defined as $u(2L_0) = 2\varepsilon_p L_0$ in an absolute coordinates.
- The initial conditions for the phase fractions are defined, being the geometry in austenite phase ($x_A = 1$, $x_{M-} = 0$, $x_{M+} = 0$).

As it has been explained, there are some parameters that are necessary to run the model. The parameters are related to the spring stiffness and the beam's material. Those parameters are calculated in Section 5.3. Moreover, the necessary tests for the model validation are explained in detail in the next section.

5.3 Experimental

This section shows the necessary parameters for the model in order to run the antagonistic model, describing the tests performed to get them. Moreover, some tests were done on the real actuator to be compared with the simulation data. This comparison allowed to know the model behaviour versus the real behaviour, in order to validate the model. Therefore, this section is divided in two parts: Experimental parameters for an antagonistic model, and Comparative tests on an actuator.

5.3.1 Experimental for an antagonistic model: 3 points bending test

In order to run the COMSOL model, some parameters were required in the software. Some of them are provided by the manufacturer, as the material properties and specific heat, and the parameters for the single wire model calculated in Section 3.3, as $T_L, E_A, E_M, \sigma_L, \Delta\sigma_L, \sigma_R$ and ε_T. Those model parameters were obtained from two isothermal tests at different temperatures, and were the same that the parameters for a single implementation (Table 3.3). However, a new parameter appears for the antagonistic implementation, as has been seen in Section 5.2: the effective spring stiffness (K_{beam}).

As it has been seen in Equation 5.8, the effective spring stiffness depends on the actuator moment of the inertia (I_{act}), the distance to the neutral axis (a), the cross-section (A_{SMA}), and the actuator Young's modulus (E_{act}). All the parameters were known, except the Young's modulus of the actuator. The actuator has been manufactured in APA-6 and its elasticity modulus has been determined experimentally. The actuator was tested with a three point bending test, with the Mechanical Testing System (MTS). This test can be seen in Figure 5.5.

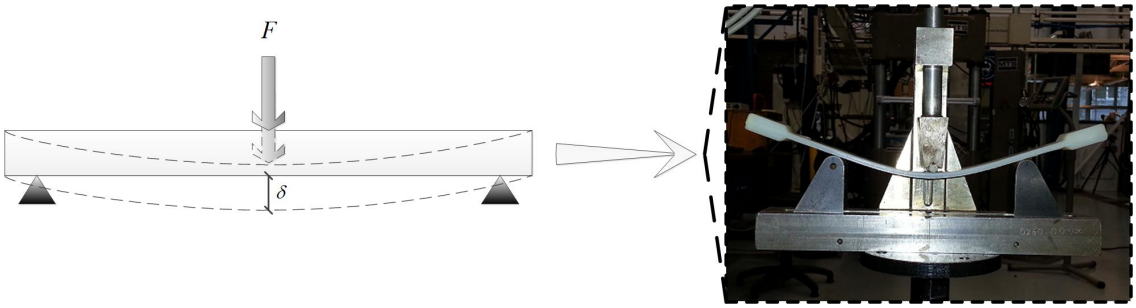

Figure 5.5: Actuator tested on a three bending test in the MTS.

The displacement depends on the force applied and the material properties, and is given by:

$$\delta = \frac{FL^3}{48E_{act}I_{act}} \tag{5.12}$$

where F is the force applied, L the distance between the supports, I_{act} the modulus of the inertia, and E_{act} the Young's modulus. The modulus of the inertia depended on the actuator geometry and the MTS provided the relationship between the force applied and the displacement undergone, just E_{act} was unknown. Thus, the Young's modulus was calculated by Equation 5.13.

$$E_{ACT} = \frac{FL^3}{48\delta I_{act}} \tag{5.13}$$

The actuator tested is shown in Figure 5.6, where can be seen its geometry and dimensions.

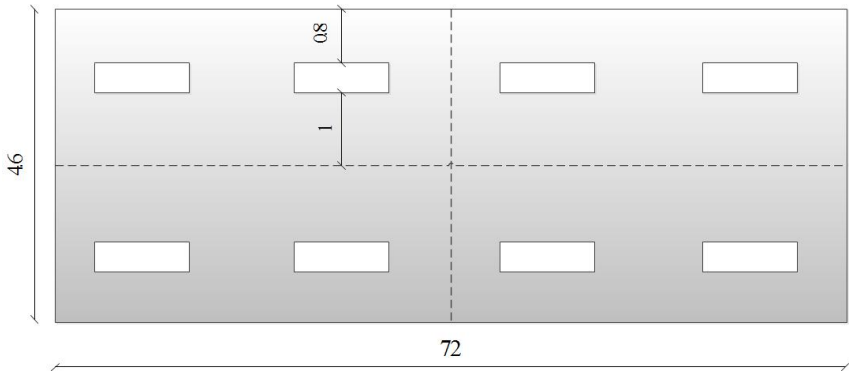

Figure 5.6: Schema of the beam tested on MTS

Following Figure 5.6, the modulus of the inertia was calculated by:

$$I_{ACT} = I_{beam} - 8\left(I_{channel} + A_{channel}d^2\right) \tag{5.14}$$

where

$$\begin{cases} I_{beam} = \dfrac{1}{12}\left(b.h^3\right) \\ I_{channel} = \dfrac{1}{12}\left(b_{channel}.{h_{channel}}^3\right) \\ A_{channel} = b.h \\ d = offset \end{cases} \tag{5.15}$$

5.3.2 Comparative tests on an actuator

The goal of this section is to do a test with the antagonistic setup, getting the deflection-strain and temperature-strain relationships. This kind of tests provided the data to be able to compare them with the simulation results. The main result of this test was the relationship between the deflection and the strain, where the beam influence could be analysed. Thus, the temperature-strain relationship was a secondary result and was not able to obtain it, as is explain below.

Initially, the test was done by implementing the real behaviour on the trailing edge of the flap, as has can be seen in Figure 5.1. Here, the actuator was tested in a horizontal position clamped on it without any flap frame. The main input in this configuration was the power, controlling the temperature of the wires and, consequently, the deflection of the actuator. Moreover the aperture of the valve was another input, used to control the different cooling rates. Those outputs on the system were collected with the same equipment than the previous configuration, an infrared camera for the temperature and a LVDT for the displacement. A schema of this configuration is shown in Figure 5.7.

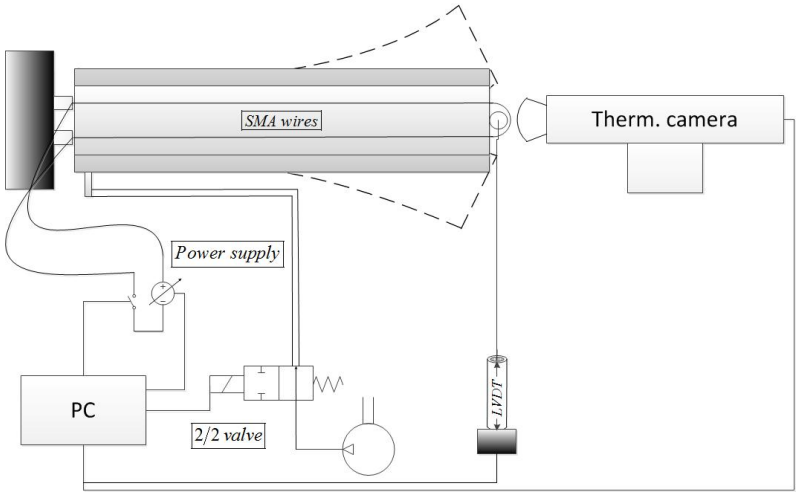

Figure 5.7: Schematic of the antagonistic setup

During this test, an unexpected problem appeared on the system. The temperature was measured on wire, where the wire starts the way back. On that point, the temperature decreased significantly, comparing it with its real behaviour studied in Chapter 4 (isothermal test). This strange behaviour of the temperature could be also checked in others points of the system. The temperature was also measured close to electrical clamps, getting the same result. Those temperatures at different points were checked with a thermocouple without any changes. The SMA wire has changes of the temperature when the temperature is measured close to the points with maximum stress, decreasing it more than 60 degrees. This aspect is not clear at all, being one of the future points of study in this project. Therefore, it was not possible to measure the temperature - strain relationships.

Only the deflection-strain relationship could be measured. This was obtained in a previous work on this Project [8]. This test was done with a previous version of the actuator(Figure 5.10), in which channels are circulars and its length is 210mm. This experiment provided the deflection on the actuator for different applied load on one wires. The deflection could be related to the wire contraction geometrically. Thus, the beam influence on the system could be analysed. The actuator was tested using a grip to hold it vertically. Moreover, the SMA wires were replaced by steel wires to avoid elasticity. A support was installed to hold the weights on the wire. A laser was also installed (200mm laser range) to measure the actuator displacement depending on the weights. More detail about this test are explained in the technical report [8]. Figure 5.8 shows a picture of the test.

Figure 5.8: Actuator deflection under a load applied [8]

As it has been described, the spring stiffness and deflection-strain relationship could be analysed. The results provided by those tests are shown in Section 5.4.

5.4 Results and Discussion

This section discusses the results obtaned in the previous section. Following that section, the parameters for the antagonistic model are obtained, as well as the tests on the actuator. This section is divided in three parts: the first one describes the parameters obtained for the model, the second one the test to analyse the beam influence and the comparison with the simulation, and the last one the validation of the antagonistic model.

5.4.1 Parameters: E_{beam}

Following the process in Subsection 5.3.1, the only unknown parameter was the E_{beam}. The other parameters were listed on Table 3.3. In other obtain the spring stiffness, the modulus of the inertia of the actuator used was calculated, as has been shown in Figure 5.6. Replacing Equation 5.20 with the real values

$$\begin{cases} I_{beam} = \dfrac{1}{12}\left(0,072.0,0046^3\right) = 584,016.10^{12}m^4 \\ I_{channel} = \dfrac{1}{12}\left(0,01.0,0005^3\right) = 1,042.10^{-13}m^4 \\ A_{channel} = 0,0005.0,01 = 5.10^{-6}m^2 \\ d = 0,00125m \end{cases} \tag{5.16}$$

the modulus of the inertia is calculated, whose value is $I_{ACT} = 520,6824.10^{12}m^4$.

Moreover, the force - displacement relationship from the MTS was analysed and calculated as

$$\frac{F}{\delta} = 10945N/m \tag{5.17}$$

The length between the support was 13.2mm of length. Once all the parameters were obtained, the Young's modulus was calculated. Its value is $E_{ACT} = 1,007.10^9Pa$.

5.4.2 Actuator influence in an antagonistic setup

This previous work was done for different weights, from 1kg to 15kg, analysing the deflection on the actuator, as well as the wire contraction. A summary of those data are shown in Table 5.1.

Mass [kg]	Actuator deflection[mm]	Wire displ. [mm]	strain [ ]
1	6.41	0.04	1.82E-3
2	12.91	0.08	3.65 E-3
3	19.35	0.11	5.47 E-3
4	26.19	0.16	7.39 E-3
5	32.92	0.19	9.26 E-3
6	40.85	0.24	1.144 E-2
7	50.24	0.29	1.398 E-2
8	57.88	0.34	1.601 E-2
9	65.41	0.38	1.797 E-2
10	74.16	0.42	2.021 E-2
11	81.71	0.46	2.209 E-2
12	94.02	0.53	2.506 E-2
13	104.83	0.58	2.756 E-2
14	118.53	0.64	3.059 E-2
15	133.15	0.71	3.364 E-2

Table 5.1: Actuator deflection for different weights [8]

Those data provided the relationship between the weights and the strain of the wire. This relationship could not be compared with the simulation results directly. In order to be able to analyse both results, a fitting equation was found. This equation was gotten from the first six weight - strain values, and is given by Equation 5.18, as can be seen in Figure 5.9.

$$y = 5287.3x + 0.0529 \tag{5.18}$$

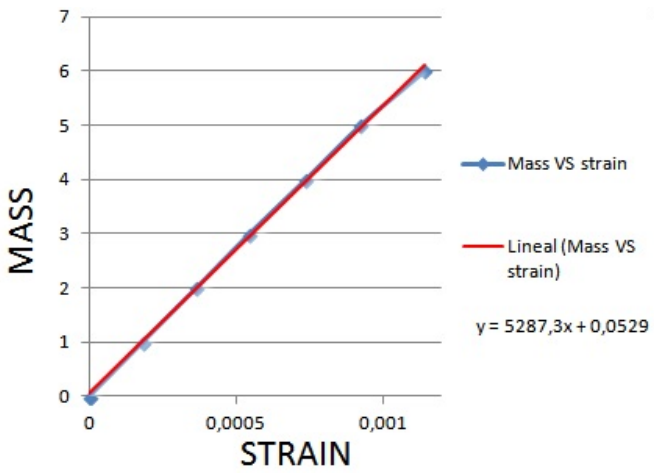

Figure 5.9: Fitting of the mass - strain relationship [8]

In order to be able to compare the experimental data with the simulations, the same actuator was studied. The actuator used in the deflection - strain test was the one with four circular channels. The section is also smaller than the actuator described previously. A schema with this new geometry is shown in Figure 5.10.

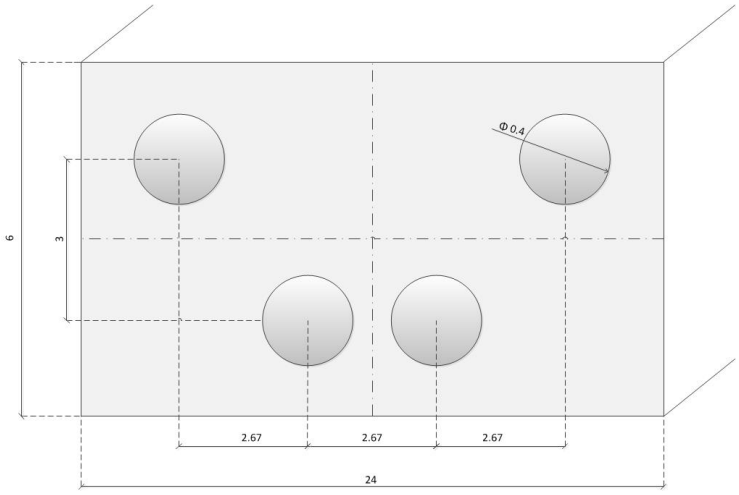

Figure 5.10: Schema of a actuator tested in the beam influence study

Moreover, the modulus of inertia of this new actuator is calculated, and given by

$$I_{ACT2} = I_{beam2} - 4\left(I_{channel2} + A_{channel2}{d_2}^2\right) \tag{5.19}$$

where

$$\begin{cases} I_{beam2} = \dfrac{1}{12}\left(b.h^3\right) = \dfrac{1}{12}\left(0,024.0,006^3\right) = 4,32.10^{-10}m^4 \\ I_{channel2} = \dfrac{1}{4}\pi.r^4 = \dfrac{1}{4}\pi.\left(\dfrac{0,0018}{2}\right)^4 = 5,1533.10-13m^4 \\ A_{channel2} = \pi.r^2 = \pi.\left(\dfrac{0,0018}{2}\right)^2 = 2,54.10^{-6}m^4 \\ d_2 = \dfrac{3}{2} = 1,5.10^{-3}m \end{cases} \tag{5.20}$$

Replacing the values, the moment of inertia is $I_{ACT2} = 4,07.10^{-10}m^4$.

5.4.3 Validation

Calculated the parameters for the antagonistic model, the model is run. Those parameters simulated the real behaviour on the actuator, being controlled by Joule effect. The input in the software was a trapezoidal signal, limited to 4W of power and 100s of period. Thus, three cycles were done without any forced air (only natural convection). Unfortunately, the model did not converge in any solution. After that, a complete study about the model was done in order to converge in a solution. A tuning parameter (TP) was found and the model converged properly.

Once the model converged in a solution, the results could be compared with the experimental data. This tuning parameter was found in relation with the beam influence, decreasing it. This involved that the beam influence is much bigger than the real one for the model, because this influence must be divided by $TP = 11000$. Thereby, the results were comparable. The tuning parameter and the strain gotten from the simulation is

$$K'_{beam} = \frac{K_{beam}}{TP} = \frac{K_{beam}}{11000} \tag{5.21}$$

In those results, the maximum and minimum strains on the wire were obtained, as well as the equivalent weight to obtain that strain. Those weights were calculated by Equation 5.18. As it

Minimum value	ux_{min}	$2,1.10^{-5}$ [ ]	$Mass_{min}$	$0.163kg$
Maximum value	ux_{max}	$9,8.10^{-4}$ [ ]	$Mass_{max}$	$5.234kg$

Table 5.2: Simulation results for antagonistic setup

has been described previously, this equation shows the weight-strain relationship, which is related with the deflection directly. Those results are shown in Table 5.2.

The strain of the real wire was calculated geometrically from the antagonistic test. The test was done following Figure 5.7 without the infrared camera. Only the deflection on the actuator was measured and, consequently, the strain provided on the wire. Figure 5.11 shows how this strain has been obtained.

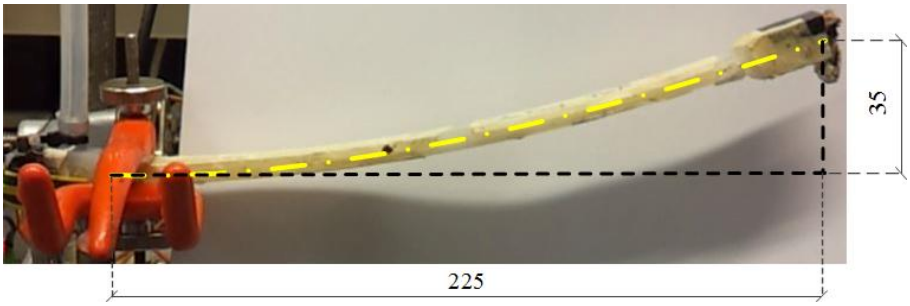

Figure 5.11: Antagonistic behaviour: real deflection on the beam

As it can be seen in the figure, the maximum lineal deflection is $0.035m$ when the actuator is working in an antagonistic configuration. This deflection was calculated for the maximum contraction on the wire. Thus, the weight and strain equivalents for that deflection could be calculated, using Equation 5.18. Summarizing, those results are

$Mass$	$5,25kg$
$Strain$	$9,83.10^{-3}$[ ]

Table 5.3: Experimental results for antagonistic setup

Comparing the experimental and simulation results, the antagonistic model can be validated. Both results show a similar wire behaviour, where the maximum recoverable strains are very similar. Thus, the equivalent weights that achieve the deflection are in the same range, whose difference is $0.016kg$. It can be concluded that the antagonistic model shows a good behaviour, being able to simulate the actual actuator. The model can be used to implement different situations, fitting it clearly to the real deflection. The tuning parameter was determined by trial and error simulations. This parameter includes also the differences between the simulation and the experiment, due to the fact that the same test could not be done because the temperature on the free end took a strange behaviour. The previous work that calculated the deflection [8] did not take into account the wire behaviour on the other side of the neutral axis. This wire should be opposed to the deflection in the opposite side. Thus, the deflection is delimited by this wire, decreasing it. This reason explains that the tuning parameter took a higher value to fit the results to that deflection. It has not been possible in this Thesis analyse other ways to improve the model, decreasing this parameter.

Summarizing, some new tests can be done in a future work. In order to get a better model, the same test must be implemented, such as checking the temperature on the wire in the middle of the actuator. Thus, equivalent tests could be compared, analysing the tuning parameter influence. Once the study of this model was done, some test can be done obtaining the actuator behaviour

for different situations. Those tests can compare the antagonistic model, checking the validity of this model.

5.5 Conclusions

In order to validate the antagonistic model, some aspects have been described in this chapter. Following the single wire model, the antagonistic setup was developed. The Müller - Achenbach - Seelecke model was used [4, 18], implementing the antagonistic model as Veeramani et al. explains in [23]. The necessary parameters for the model were calculated. Some of them were imported from the single wire model, and the spring stiffness obtained in an experimental test. The three bending test was done and this parameter obtained. Moreover, the actuator influence was determined as has been described in [8]. The deflection of the actuator was related with the hung weight and, geometrically, the strain produced on the SMA wire.

With all the parameters, the antagonistic model was implemented and run. Those results were compared with the deflection data, showing a good agreement with the simulation. The model could be validated comparing those cases. However, in order to run the model properly, a tuning parameter was necessary. This parameter affects to the actuator influence, forcing it to minimize its influence.

Summarizing, the model was validated according to the experimental data. But this model must be improved in order to study the influence of all the model parameters. Thus, the tuning parameter could be minimized or removed, simulating the real antagonistic behaviour.

Chapter 6

Conclusions

This chapter gathers the achieved goals in this Thesis. As it has been described, this Thesis is focused on the trailing edges of the flap. In order to modify its geometry, Shape Memory Alloys were embedded in an actuator, so that a deflection of the actuator can be induced. The goal of this Thesis was to describe the Shape Memory Alloy behaviour and develop a model that was able to predict its behaviour. In addition, the performance of the material was studied and compared with the model results. Those tests confirm that the active cooling is the limiting factor for the actuation. A summary of those goals are shown here.

The first point of this Thesis has been the development of a model for a SMA. This model has been implemented in COMSOL (Chapter 3). In order to run and compare the model wire with the real one, some parameters were required. Some of them were provided by the manufacturer, others were obtained geometrically in an isothermal test, and the rest of the parameters in a isobaric test. The isobaric test was done for different airflows, showing the heat transfer coefficient-airflow relationship. This relationship shows the importance of the active cooling, where the maximum h_{conv} is 8.5 higher than the natural convection. The importance of the active cooling has been demonstrated in a thermal study, where the convective heat transfer is the most important of the system. Its influence is more than the 90% of the total. Once the isothermal and isobaric test were done, the model was run and compared with the experimental results. The model shows a good agreement with experimental results, fitting properly for different temperatures.

Once the single model was validated, different isobaric tests were done and compared with the model results for weights from 1kg to 6kg. The heating and cooling responses were studied, calculating the time that takes for the wire to be contracted and elongated. Their combination provide the maximum working rate. It is maximum for the highest power and airflow. The maximum experimental working rate is $0.12Hz$, whereas the simulation is $0.45Hz$. The simulation has faster responses that the experimental results , because the heating and cooling time are shorter. Some inaccuracies could be appreciated in both results, due to the model implemented. This model is monocrystalline, whereas the actual wire is polycrystalline. Therefore, the model has faster responses. Moreover, the best strain range was determined around the midpoint of the strain. Around this point the highest responses were obtained due to the transformation phases happens in the middle of the full strain range. This attainable frequency is almost 3.5 times higher at the midpoint reference that the minimum reference for same conditions of power and airflow.

Following the single model, the antagonistic model has been implemented and validated. In order to get comparable results, a tuning parameter was necessary. This parameter affects to the actuator influence, by reducing it. This parameter is one of the future work in order to be improved the model. Those results show that the simulation wire is $9.8.10^{-4}$ of the strain, whereas the actual wire is $9.83.10^{-3}$. That means that the strain produced is similar in both cases, as well as the mass equivalent.

Summarizing, this Thesis is focused on the Shape Memory Alloy. Thus, its behaviour is studied and implemented in a software in two ways: single wire and antagonistic setup. The

single wire model has been validated and used for different simulations, comparing the results with experimental tests. The antagonistic model was implemented with a tuning parameter. This model must be improved in order to study the influence of all the model parameters. Moreover, similar tests have to be done, being able to compare the experimental and simulation results.

Bibliography

[1] Company founded in the design of a shape-morphing adaptive control surface of an airfoil. 3, 5

[2] European aeronautical research programme, which mission is to develop breakthrough technologies to significantly increase the environmental performances of airplanes and air transport with public - private partership. 3, 5

[3] J.A. Garcia-Manrique A. Alfonso, J. Andres. Synthesis of APA6 thermoplastic matrices for the manufacture ofgreencomposites. *AIP Publishing*, 2012. 11

[4] Manfred Achenbach. A model for an alloy with shape memory. *International Journal of Plasticity*, 5(4):371 – 395, 1989. 13, 42, 53

[5] David Ayuso-Garrido. Modelling a Shape Memory Alloy Actuator to be implemented as a Morphing Trainling Edge. Master's thesis, TU Delft, 2012. viii, 2, 5, 9

[6] John H Crews and Gregory D Buckner. Design optimization of a shape memory alloy - actuated robotic catheter. *Journal of Intelligent Material Systems and Structures*, 23(5):545–562, 2012. 15

[7] John H Crews, Ralph C Smith, Kyle M Pender, Jennifer C Hannen, and Gregory D Buckner. Data-driven techniques to estimate parameters in the homogenized energy model for shape memory alloys. *Journal of Intelligent Material Systems and Structures*, 23(17):1897–1920, 2012. 13, 16, 17

[8] Bruno Giuntoli. Dynamic control of composite flap with embedded sma actuation wires. Technical report, TUDelft, 2013. ix, x, 48, 49, 50, 52, 53

[9] Olaf Heintze. *A Computationally Efficient Free Energy Model for Shape Memory Alloys - Experiments and Theory.* PhD thesis, North Carolina State University, Dec - 2004. 13

[10] Ahmed Kamel. Characterization of Shape Memory Alloys and Manufacturing of Shape Memory Alloys based Actuators for "Smart Fixed-Wing Aircraft". Technical report, 2012. viii, 9, 10

[11] Dimitris C. Lagoudas. *Shape Memory Alloys: Modeling and Engineering Applications.* Spinger, 2008. viii, 6, 7, 8, 13

[12] Adrian Lara-Quintanilla. Manufacturing and Control of Shape Memory Alloys (SMA) Based Actuators. Master's thesis, TU Delft, 2010. viii, 11, 12

[13] Adrian Lara-Quintanilla. Experimental and finite element analysis on an SMA-based actuator for aerodynamic load control on aircraft wings. ICAST2013, NOV 2013. viii, 17, 18

[14] Adrian Lara-Quintanilla, Anton W Hulskamp, and Harald EN Bersee. A high-rate shape memory alloy actuator for aerodynamic load control on wind turbines. *Journal of Intelligent Material Systems and Structures*, 2013. viii, 10, 11, 12

[15] Qifu Li. *Modeling and Finite Element Analysis of Smart Materials*. PhD thesis, 2006. 14

[16] Jordan E. Massad and Ralph C. Smith. A homogenized free energy model for hysteresis in thin-film shape memory alloys. *Thin Solid Films*, 489(12):266 – 290, 2005. 14

[17] Jose Luis Pons. *Emerging actuator technologies: a micromechatronic approach*. 2005. 5, 6

[18] Stefan Seelecke and Ingo Mller. Shape memory alloy actuators in smart structures: Modeling and simulation. *Applied Mechanics Reviews*, 57(1):23–46, February 2004. 13, 42, 53

[19] Kenneth Wayne Smith. Fighter Aircraft Synthesis - Design Optimization. Master's thesis, 2009. viii, 3

[20] Gregory Ervin-Dragan Maric Sridhar Kota, Russell Osborn. Mission adaptive compliant wing design, fabrication and flight test. viii, 3, 4

[21] Peter Flick-Carl Tilmann Sridhar Kota, Ed Pendleton. Design and application of compliant mechanisms for morphing aircraft structures. viii, 4

[22] Julie JE Teuwen, AA van Geenen, and Harald EN Bersee. Vacuum-infused anionic polyamide-6 composites: The effect of postprocessing. *Journal of Thermoplastic Composite Materials*, 25(8):965–986, 2012. 11

[23] Arun S Veeramani, Gregory D Buckner, Stephen B Owen, Richard C Cook, and Gil Bolotin. Modeling the dynamic behavior of a shape memory alloy actuated catheter. *Smart Materials and Structures*, 17(1):015037, 2008. 42, 43, 53

Appendix A

Isothermal Test

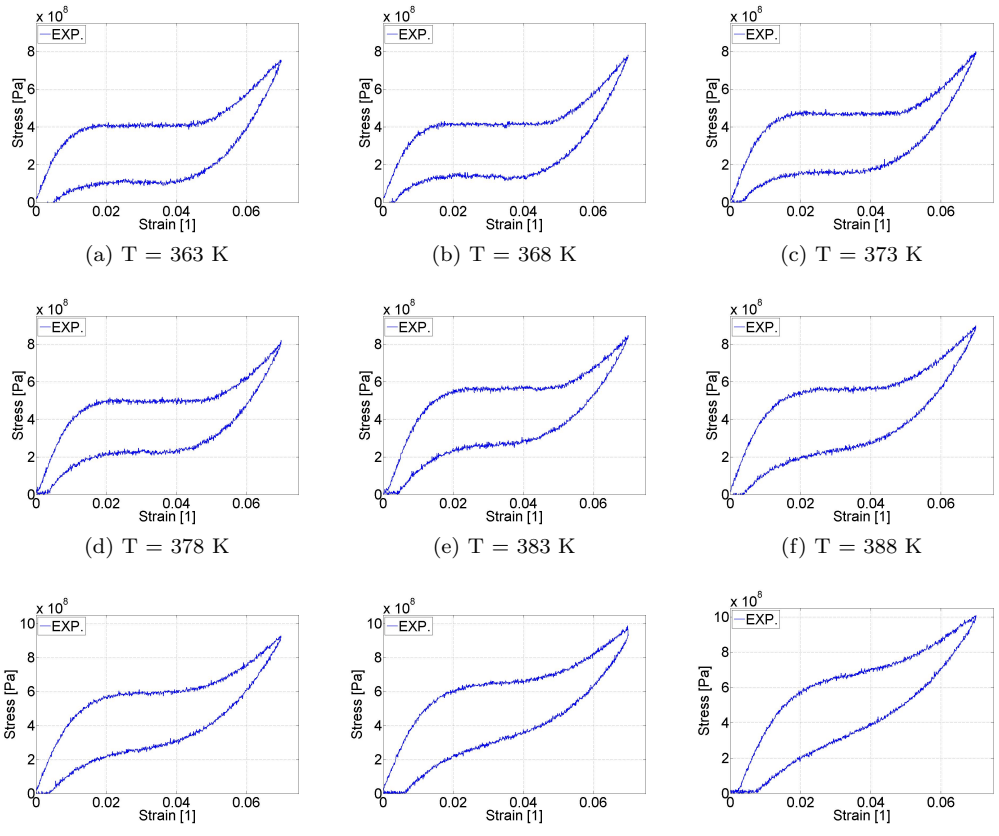

(a) T = 363 K (b) T = 368 K (c) T = 373 K

(d) T = 378 K (e) T = 383 K (f) T = 388 K

(g) T = 393 K (h) T = 398 K (i) T = 403 K

Figure A.1: Isothermal test with laboratory data, every temperatures

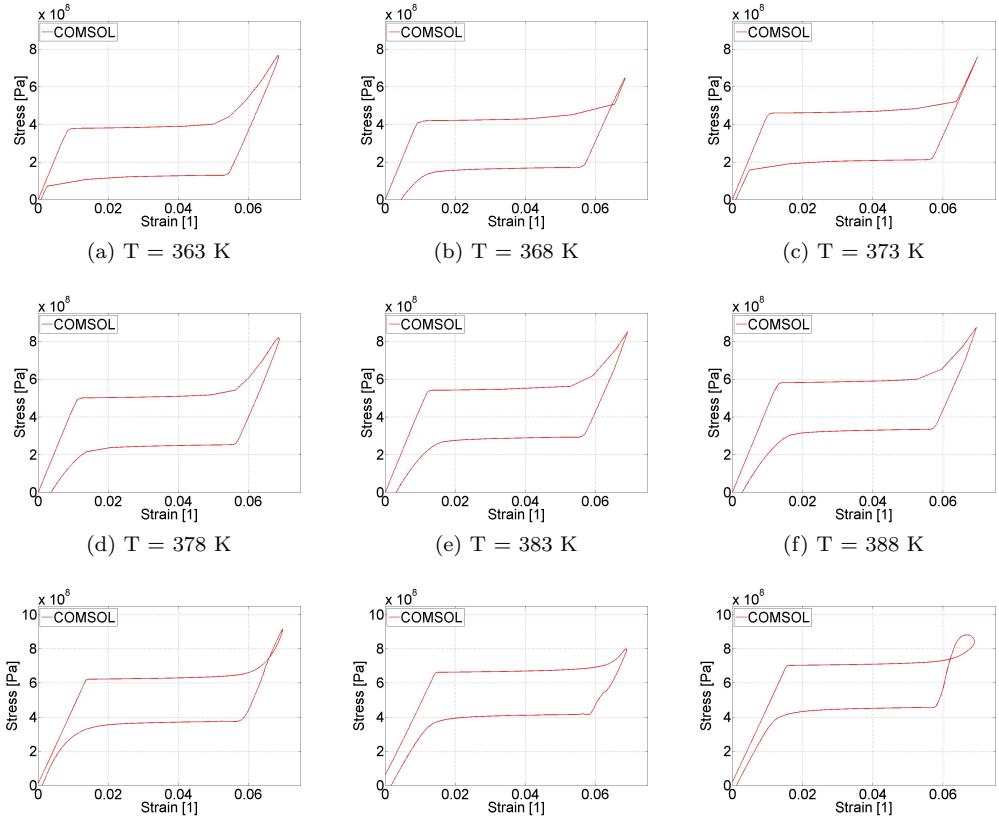

(a) T = 363 K (b) T = 368 K (c) T = 373 K

(d) T = 378 K (e) T = 383 K (f) T = 388 K

(g) T = 393 K (h) T = 398 K (i) T = 403 K

Figure A.2: Isothermal test with COMSOL data, every temperatures

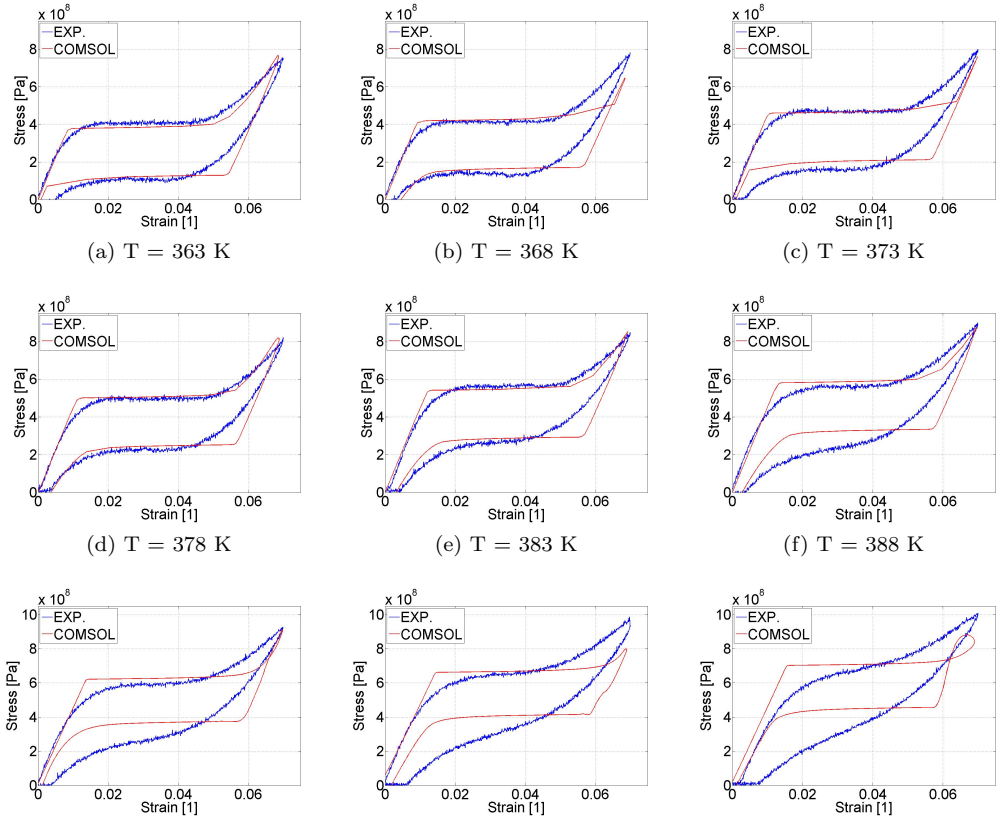

(a) T = 363 K (b) T = 368 K (c) T = 373 K

(d) T = 378 K (e) T = 383 K (f) T = 388 K

(g) T = 393 K (h) T = 398 K (i) T = 403 K

Figure A.3: Validation of isothermal test (laboratory and COMSOL), every temperatures

Appendix B

Working rate

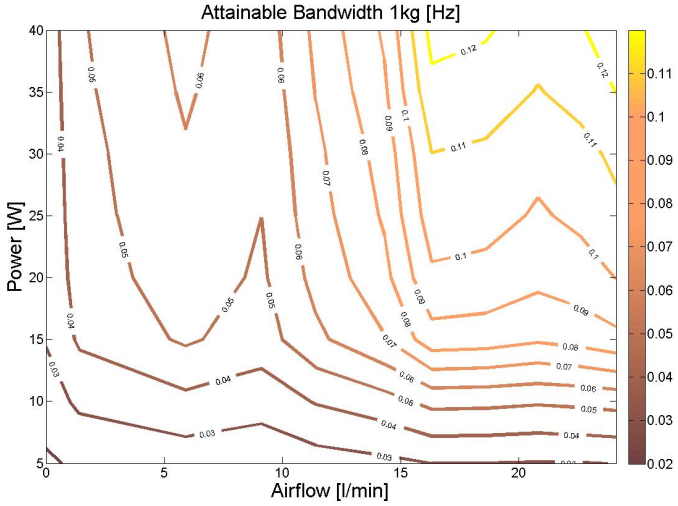

(a) M = 1 kg

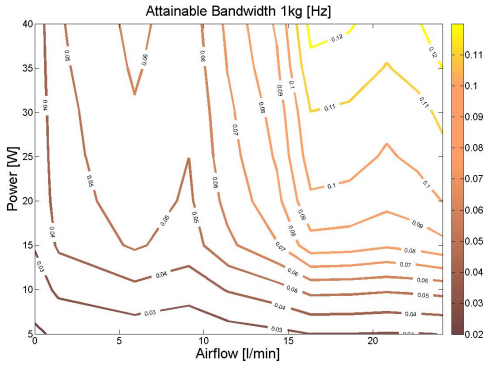

(b) M = 2 kg

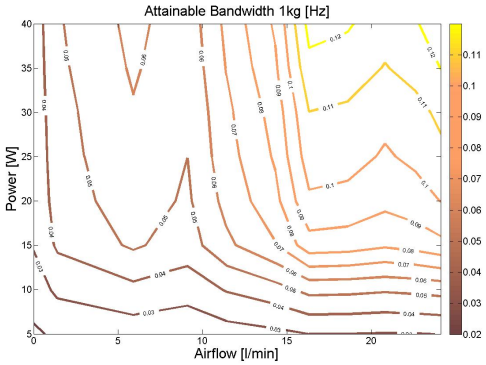

(c) M = 3 kg

Figure B.1: Attainable actuator working rates (Hz) in experimental data

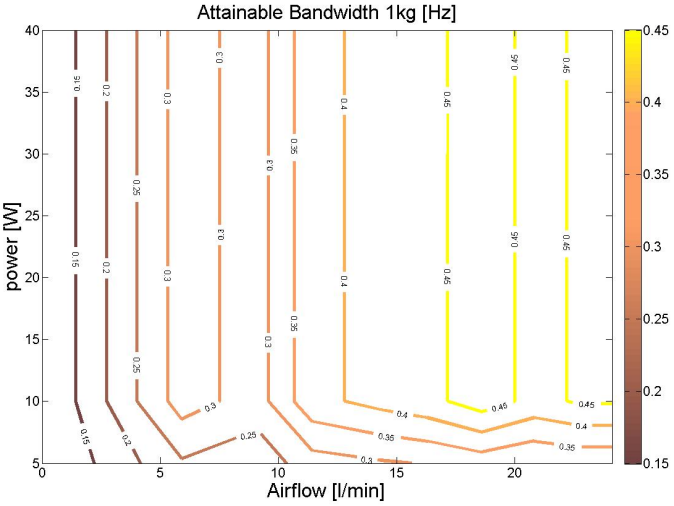

(a) M = 1 kg

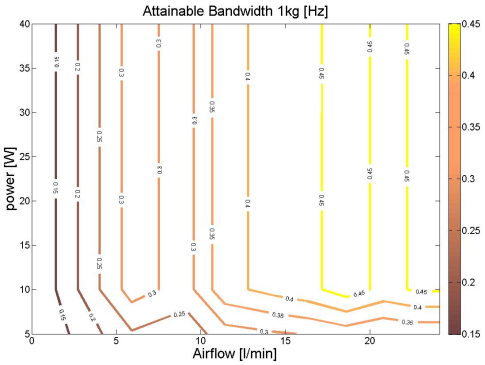

(b) M = 2 kg

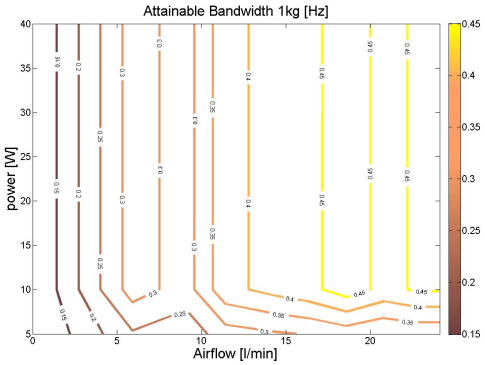

(c) M = 3 kg

Figure B.2: Attainable actuator working rates (Hz) in model data